# Diffuse Venting and Near Seafloor Hydrothermal Circulation at the Lucky Strike Vent Field, Mid-Atlantic Ridge

**Benjamin Wheeler[1]** , **Mathilde Cannat[1]** , **Valérie Chavagnac[2]** , and **Fabrice Fontaine[1,3]**

[1]Institut de Physique du Globe de Paris, Université Paris Cité (IPGP), UMR 7154, CNRS, Paris, France, [2]Géosciences Environnement Toulouse (GET) UMR 5563, CNRS, Observatoire Midi-Pyrénées, Université de Toulouse, Toulouse, France, [3]Observatoire Volcanologique du Piton de la Fournaise (OVPF), La Réunion, France

**Abstract**   We report on a 3 years monitoring experiment of low to medium temperature diffuse venting at two vent sites (Tour Eiffel and White Castle) of the Lucky Strike, black smoker-type hydrothermal field, Mid-Atlantic Ridge. Diffuse vents account for a large part of the energy flux of mid-ocean ridges hydrothermal fields and provide key habitats for the hydrothermal fauna. We document the time and space variability of diffuse venting temperature and chemistry, describe the effect of tidal loading and currents and discuss the extent of mixing, cooling of black smoker fluids, heating of entrained seawater and anhydrite precipitation/dissolution in the substratum. We emphasize the role of a thin (<2 m) volcaniclastic formation capping the brecciated basalt substratum. This formation is porous, but becomes impermeable when indurated by hydrothermal precipitates. It forms an intermediate layer between the vents at the seabed and the fluids as they discharge out of the brecciated basalts. Diffuse fluids inferred to discharge out of meter-spaced cracks in the brecciated basalts beneath this volcaniclastic layer are hot (>80°C) and contain >10% of the hot endmember fluid component, over distances of up to 25 m from the black smokers. These results provide a geologically integrated framework in which to study site-scale, near seafloor hydrothermal circulation and associated vent habitats at Lucky Strike and other black smoker-type hydrothermal fields. They suggest diffuse heat fluxes in the upper range of previously published estimates at the two studied Lucky Strike hydrothermal vent sites.

**Plain Language Summary**   Mid-ocean ridges (MOR) are a key feature of plate tectonics, extending some 60,000 km in all the major oceans. MOR hydrothermal circulations transfer heat and chemical compounds from the solid earth to the ocean and provide habitats for the hydrothermal fauna. The vents include black smokers that expel the hottest fluids and diffuse vents that expel lower temperature fluids at lower rates but over larger surfaces. The contribution of diffuse vents to the energy and chemical fluxes of MOR hydrothermal systems is still largely an open question. In this paper, we address it by using data from a 3 years monitoring experiment of diffuse vents at two sites (Tour Eiffel and White Castle) of the Lucky Strike, a black smoker-type hydrothermal field in the Mid-Atlantic Ridge. We document the time and space variability of venting temperature and derive chemical constraints on the extent of mixing of black smoker fluids with entrained seawater and of mineral precipitation/dissolution in the substratum of the vents. Our results suggest diffuse heat fluxes in the upper range of previously published Lucky Strike hydrothermal field estimates and provide a geologically integrated framework in which to study diffuse vent habitats at Lucky Strike and other black smoker-type hydrothermal fields.

## 1. Introduction

Hydrothermal circulation at mid-ocean ridges transfers most of the magmatic heat associated with the accretion of newly formed oceanic crust (Cann & Strens, 1982; Lister, 1972; Lowell et al., 1995) and is one of the main vectors for chemical exchanges between the lithosphere and the hydrosphere (Alt, 1995; Elderfield & Schultz, 1996). Mid-ocean ridge (MOR) black smoker hydrothermal systems result from km-scale hydrothermal cells in which seawater percolating down is progressively modified through reactions with the host rocks and mines magmatic heat at depth (Alt, 1995; Lister, 1974; Wilcock & Delaney, 1996). These km-scale cells result in localized fluid discharges carrying reduced chemical compounds that are a source of energy for unique chemosynthetic ecosystems. Venting occurs in the form of focused vents called smokers (Edmond et al., 1995; Gamo et al., 1996) and of diffuse vents that expel lower temperature fluids but extend over larger surfaces (Baker et al., 1993; Barreyre

**Investigation:** Benjamin Wheeler, Mathilde Cannat, Valérie Chavagnac, Fabrice Fontaine
**Methodology:** Benjamin Wheeler, Mathilde Cannat, Valérie Chavagnac
**Project administration:** Mathilde Cannat
**Resources:** Mathilde Cannat
**Software:** Benjamin Wheeler, Mathilde Cannat
**Supervision:** Mathilde Cannat
**Validation:** Benjamin Wheeler, Mathilde Cannat, Valérie Chavagnac
**Visualization:** Benjamin Wheeler, Mathilde Cannat
**Writing – original draft:** Benjamin Wheeler, Mathilde Cannat
**Writing – review & editing:** Benjamin Wheeler, Mathilde Cannat, Valérie Chavagnac, Fabrice Fontaine

et al., 2012; Bemis et al., 2012). Because of their larger surface extent, diffuse vents are estimated to contribute 50%–95% of total MOR hydrothermal heat fluxes (Baker et al., 1993; Mittelstaedt et al., 2012; Ramondenc et al., 2006; Schultz et al., 1992). They expel fluids at temperatures that allow the growth of microbial faunal communities and therefore also play a prevalent role in hosting the hydrothermal life (Corliss et al., 1979; Cuvelier et al., 2009; Holden & Daniel, 2004; Jannasch & Mottl, 1985; Juniper et al., 1995).

Focused vent fluids form sulfide chimneys, mounds and flange structures (Tivey, 2007). Diffuse vents are diverse, depending on the geology of the substratum and on their distance from the focused discharges (Bemis et al., 2012). They occur in cracks (Barreyre et al., 2012; Butterfield et al., 2004; Embley et al., 1990; Glickson et al., 2007; Mittelstaedt et al., 2016; Sohn, 2007; Tivey, 2007), flanges and diffusers (Tivey, 1995). Patches of diffuse venting, revealed by the presence of microbial mats, occur in porous substrates, such as pelagic sediments (Little et al., 1988) or, in the case of the Lucky Strike vent field, in volcaniclastic deposits (Barreyre et al., 2012). Venting velocities range between 20 and 330 cm/s at focused vents (Converse et al., 1984; Ginster et al., 1994; Mittelstaedt et al., 2012; Ramondenc et al., 2006; Rona & Trivett, 1992) and between 0.1 and 20 cm/s at diffuse vents (Cooper et al., 2000; Mittelstaedt et al., 2012; Rona & Trivett, 1992; Sarrazin et al., 2009).

Diffuse venting fluids result from interactions in the shallow substratum between the uprising hot, end-member, black-smoker-type fluids and cool percolating seawater. These interactions may include mixing of end-member fluids with seawater (Butterfield et al., 2004; Edmond et al., 1979; Kelley et al., 2002), conductive cooling of end-member fluids and/or conductive heating of the seawater (Cooper et al., 2000), sulfide precipitation (Butterfield et al., 2004), anhydrite and silica precipitation or dissolution (Cooper et al., 2000; Fouquet et al., 1994; James & Elderfield, 1996; Tivey, 1995; Tivey & Delaney, 1986), biotic and abiotic oxidation of $H_2S$ (Butterfield et al., 2004; Koschinsky et al., 2002) and microbial activity producing methane (Butterfield et al., 2004; Von Damm & Lilley, 2004) and other organic species (Foustoukos et al., 2009). Analytical and numerical models of black smoker type MOR hydrothermal systems, scaled to the dimensions of individual hydrothermal sites (several tens to a few hundred meters), aim to identify the parameters that control these near seafloor processes. Key parameters are the permeability of the substratum and the diameter of the vertical conduit of high temperature and high flow rate end-member fluids, embedded in a seawater-saturated, continuous porous medium. Some models isolate the two domains (Lowell & Yao, 2002; Lowell et al., 2003, 2012), while others allow for subseafloor mixing of end-member fluids with entrained seawater (Guo et al., 2020; Larson et al., 2015; Lowell et al., 2015). Venting of lower temperature diffuse fluids occurs when the permeability of the surrounding porous medium is at least one order of magnitude higher than that of the hot conduit (Lowell et al., 2007). However, increasing the permeability of the surrounding medium leads to the entrainment of larger volumes of cold seawater, resulting in an excessive cooling of the upwelling fluids, in conflict with the high temperatures measured at focused vents (Andersen et al., 2015; Coumou et al., 2008; Lowell et al., 2007). Anhydrite precipitation upon heating of the entrained seawater to temperatures above 150°C (Bischoff & Seyfried, 1978) is introduced as a way to locally clog the porosity, creating low permeability barriers around the central conduit and allowing for the simultaneous discharge of black smokers and diffuse venting fluids (Guo et al., 2020; Lowell et al., 2003).

Tidal signals observed in fluid temperature time-series measured at black smoker and at some diffuse hydrothermal vent sites appear to result primarily from tidal pumping (tidally modulated current velocities also cause temperature variations at some diffuse vents; Little et al., 1988; Scheirer et al., 2006; Tivey et al., 2002) and have been used to probe the poroelastic behavior and the hydrological properties of the substratum (Barreyre & Sohn, 2016; Barreyre et al., 2022; Crone & Wilcock, 2005; Jupp & Schultz, 2004; Sohn, 2007; Xu et al., 2017). Crone and Wilcock (2005) show that tidal pumping may enhance the mixing of endmember fluids and entrained seawater but cannot produce the semi-diurnal venting temperature variations >0.5°C documented at several diffuse vents (Barreyre et al., 2014a; Larson et al., 2007; Mittelstaedt et al., 2016; Scheirer et al., 2006; Tivey et al., 2002). To account for such large amplitude variations, Crone and Wilcock (2005) proposed a conceptual setup involving heterogeneous fracture-controlled permeability, impacted by tidally modulated horizontal pressure gradients.

In this paper, we present the results of a 3 years monitoring study at two representative vent sites of the basalt-hosted Lucky Strike hydrothermal field (LSHF): Tour Eiffel (TE) and White Castle (WC; Figure 1). Tour Eiffel is a large site with a ~15 m-high sulfide tower, while White Castle is smaller with a 3 m-high sulfide mound. Our study integrates seafloor mapping and geological observations at both sites, with time-series of diffuse fluid
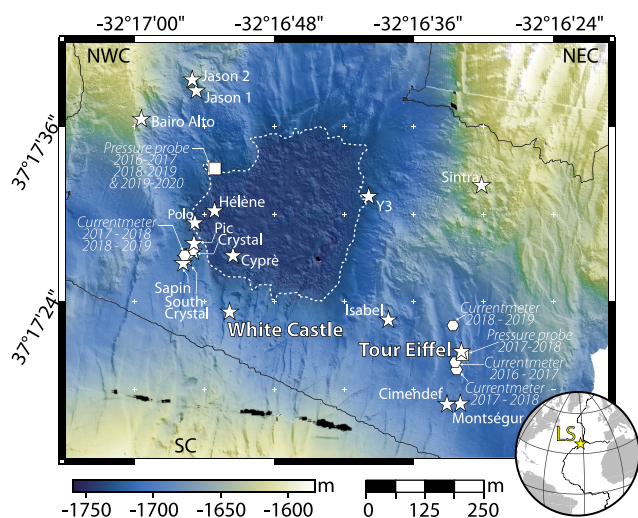
**Figure 1.** Map of the Lucky Strike hydrothermal field (LSHF). High resolution bathymetry from Ondréas et al. (2009) and Escartín et al. (2015). Hydrothermal sites (white stars), including the 2 sites studied here (Tour Eiffel and White Castle), are distributed around a fossil lava lake (white dotted line). Also shown are the location of currentmeters (hexagons) and pressure probes (squares) used in the monitoring experiment. NWC: Northwest Volcanic Cone; NEC: Northeast Volcanic Cone; SC: South Volcanic Cone.

temperature and chemistry from selected vents. The monitoring experiment we report was carried out as part of the EMSO-Azores observatory (European Multidisciplinary Seafloor and water-column Observatory; Colaço et al., 2011; Matabos et al., 2022). We expand on previous studies of diffuse vents at mid-ocean ridge black-smoker hydrothermal sites (Barreyre et al., 2014a; Butterfield et al., 2004; Cooper et al., 2000; Little et al., 1988; Mittelstaedt et al., 2012; Pruis & Johnson, 2004; Rouxel et al., 2004b) by acquiring long time series data from a large number of vents and integrating fine scale geological mapping into our interpretations. We combine time series measurements of fluid temperature in venting fractures, diffuse patches and black smokers at the two selected vent sites and repeated fluid sampling for chemical analysis. We also use time series of seafloor pressure and near seafloor current direction and velocity, high resolution mapping (Ondréas et al., 2009), photographic mosaics of the seafloor (Barreyre et al., 2012) and dive-observations using remotely operated and human operated vehicles (ROV and HOV). We document the effect of tidal loading and current velocity on venting temperatures and the chemical evidence for anhydrite precipitation and/or dissolution, subseafloor mixing, cooling, or heating of end-member hydrothermal fluids or seawater. We place these monitoring results in their geological context and propose a conceptual model for the dynamics of near seafloor site-scale hydrothermal circulation at the LSHF. We discuss the implications of these results for estimates of hydrothermal heat fluxes and for the diversity and temporal variability of hydrothermal habitats at the Lucky Strike vent field.

## 2. Geological Context

The Lucky Strike hydrothermal field (Langmuir et al., 1993) is located at the summit of a domal axial volcano, ∼8 km in diameter, at the center of the Lucky Strike segment of the mid-Atlantic ridge (Escartín et al., 2014; Humphris et al., 2002; Ondréas et al., 2009). Most active LSHF vents are distributed in and around a summit depression that is floored by a fossil lava lake (Fouquet et al., 1994; Ondréas et al., 2009). This depression is bound to the north and the south by two cone-shaped volcanoes that formed on top of the larger domal axial volcano prior to the activity of the lava lake (Humphris et al., 2002; Ondréas et al., 2009). The northern cone-shaped volcano is rifted in two; the southern one is more recent and, although faulted and fissured in its center, is not yet rifted (Figure 1). The extensively faulted and fissured domain that extends NNE-SSW in the center of both cone-shaped volcanoes is thought to have accommodated most of the recent plate divergence at this latitude (Escartín et al., 2014; Humphris et al., 2002; Miranda et al., 2005). Sheet lavas that filled the lava lake are mostly unfaulted (Ondréas et al., 2009) and overlay a discontinuous layered volcaniclastic formation, up to a few meters-thick, that rests on the pillows, lava tubes and brecciated basalts of the two cone-shaped volcanoes (Eissen et al., 2003; Ondréas et al., 2009).

The LSHF comprises at least 18 vent sites (Barreyre et al., 2012; Charlou et al., 2000; Escartin et al., 2015; Von Damm et al., 1998), each associated with a sulfide mound, bearing several focused vents (smokers) and surrounded by a semi-elliptical domain of diffuse venting. Radium-226/Ba dating of hydrothermal barite indicates that hydrothermal venting at Lucky Strike is at least 6,600 years old and the oldest sulfide deposits at Tour Eiffel are at least 3,800 years old (Sánchez-Mora et al., 2022). The heat source for hydrothermal circulation, with an estimated energy flux of 200–1,000 MW (Barreyre et al., 2012), is most likely an axial melt lens 3.5–4 km beneath the seafloor (Combier et al., 2015; Crawford et al., 2010; Singh et al., 2006). Constraints derived from the chemistry of the black smoker fluids are consistent with peak reaction conditions near the top of the axial magma chamber (Chavagnac et al., 2018; Pester et al., 2012). Microseismicity, interpreted as due to thermal cracking in the hydrothermal downflow domain, is mostly recorded within 2 km of the magma chamber roof top and in a 1-km-wide ridge-parallel corridor that corresponds to the extensively faulted and fissured domain (Crawford et al., 2013). These results point to a mostly along-axis main hydrothermal circulation mining heat from the axial magma lens depth (Crawford et al., 2013; Fontaine et al., 2014). A two layers permeability structure, with higher permeability in the upper few hundred meters of the hydrothermal domain, is supported by seismic velocity

modeling (Arnulf et al., 2014) and accounts best for the field-scale poroelastic effect of tidal loading on the temperature of end-member, black-smoker-type hydrothermal fluids (Barreyre & Sohn, 2016; Barreyre et al., 2014b, 2018).

Lucky Strike diffuse venting cracks and patches have been mapped at field-scale based on high resolution seafloor photomosaics (Barreyre et al., 2012; Mittelstaedt et al., 2012). Cooper et al. (2000) sampled diffuse fluids at several LSHF sites using the Medusa flow velocity and temperature device (Schultz & Elderfield, 1994) and proposed an origin by mixing of less than 7% endmember fluid with conductively heated seawater in the shallow substratum. Site-scale shallow circulation involving entrained seawater at LSHF sites is also supported by the large range of $\delta^{34}S$ values measured on sulfide samples, with the higher values reflecting a contribution of reduced seawater sulfate, probably in part due to bacterial metabolism (Rouxel et al., 2004a, 2004b). Published estimates of field scale (187–1,036 MW; Barreyre et al., 2012) and vent site scale (18.75 ± 2.22 MW for the Tour Eiffel vent site; Mittelstaedt et al., 2012) diffuse heat fluxes at Lucky Strike are based on mapping the horizontal footprint of mounds, patches, flanges and cracks and using available in situ fluid temperature and venting velocity measurements (Cooper et al., 2000; Mittelstaedt et al., 2012; Sarrazin et al., 2009).

## 3. Materials and Methods

### 3.1. Geology

We use video images from 27 ROV Victor 6000 dives and 5 HOV Nautile dives, carried out during the 2016–2020 maintenance cruises (https://campagnes.flotteoceanographique.fr/series/130/). Based on these videos, we document instrument deployment and recovery, fluid sampling operations and geological changes from 1 year to the next. We also use high-resolution bathymetry (Ondréas et al., 2009) and two sets of high resolution georeferenced photomosaics acquired with the OTUS (Simeoni et al., 2007) camera of the ROV Victor 6000, in black and white for a complete coverage of the field in 2008–2009 (Barreyre et al., 2012) and in color for a partial coverage of the Tour Eiffel and White Castle sites in 2018 (this study).

### 3.2. Fluid Sampling and Fluid Chemistry

We used a 200 mL titanium gas-tight syringe with a needle-like snorkel or with a bell-shaped and partly transparent funnel that ensures minimum mixing of the diffuse fluids with ambient seawater (Figure S1 in Supporting Information S1; Table 1). All fluids were filtered onboard the ship through 0.22 μm Millipore filters: we thus report dissolved element concentrations. Salinity, conductivity, pH and oxydo-reduction potential (Eh) were measured immediately (Chavagnac et al., 2023a, 2023b, 2023c, 2023d). Aliquots were then transferred into acid-cleaned plastic containers and stored in the dark at 4°C for shore-based analyses at the Geosciences Environment Toulouse (GET) laboratory. Ca, Na, K, Mg, Si, Fe, Mn, and Li concentrations were determined using a Horiba Ultima2 inductively coupled plasma atomic emission spectrometer (ICP-AES), calibrated using mono elemental solutions, multielemental solutions and IAPSO standard solution (Besson et al., 2014). Analytical precision is better than 2%. Cl, Br, and $SO_4$ concentrations were measured using anionic chromatography (Dionex ICS-2000) with a specific column for highly charged matrix (DIONEX IC AS19) calibrated at <2% analytical precision with the IAPSO seawater standard diluted 10–50 folds with Milli-Q water. Hydrothermal end-member fluid compositions are recalculated by linear extrapolation to zero-Mg using the least-square regression method (Von Damm, 1988).

### 3.3. Acquisition of Times Series Data

#### 3.3.1. Fluid Temperature

We collected data from 28 successful 1-year temperature probe deployments in venting orifices, cracks and diffuse patches at the Tour Eiffel (TE) and White Castle (WC) vent sites (Figure 2 and Table S1 in Supporting Information S1). We used high-temperature WHOI-MISO probes (HTW and HTWN), high-temperature NKE probes (HTNKE), low temperature WHOI-MISO probes (LTW), with sampling intervals between 1 and 14 min. We also used an in-house low temperature probe (LTGrad) made of two iButton (DS1922L) temperature sensors from Maxim Integrated with a sampling interval of 1 hr. All probes were positioned as deep as possible (typically 10–15 cm) inside the vents, cracks and venting patches. The temperature range, accuracy and resolution of these probes are summarized in Table S1 of the Supporting Information S1. Full data and metadata (sampling intervals,

**Table 1**
*Temperature and Chemical Characteristics of Focused and Diffuse Fluids Sampled at the Tour Eiffel (TE) and White Castle (WC) Monitoring Locations in 2016, 2017, 2018, and 2019 (See Section 3)*

| Year | In-situ T (°C) | Sample name | Position | Mg (mmol/L) | Si (mmol/L) | Na (mmol/L) | Cl (mmol/L) | Mn (µmol/L) | Fe (µmol/L) | Cu (µmol/L) | Zn (µmol/L) | Ca (mmol/L) | SO$_4$ (mmol/L) | Ba (µmol/L) | K (mmol/L) | Sr (µmol/L) | Br (µmol/L) | pH | H$_2$S (mmol/L) | P (%) (Mg) |
|---|---|---|---|---|---|---|---|---|---|---|---|---|---|---|---|---|---|---|---|---|
| **TE** | | | | | | | | | | | | | | | | | | | | |
| 2019 | 60 | M19FLU47[a] | TE-3 | 55.219 | 0.188 | 483 | 550 | 3.0 | bdl | bdl | 0.40 | 12.313 | 28.320 | 0.4 | 11.314 | 77 | 907 | 6.8 | 0.656 | 0− |
| | 60 | M19FLU48[a] | TE-3 | 53.701 | 0.168 | 495 | 549 | 2.1 | bdl | bdl | 0.29 | 12.380 | 28.290 | 0.3 | 11.424 | 75 | 903 | 6.8 | 0.513 | 0.74 |
| | 55 | M19FLU45 | TE-5 | 52.108 | 1.700 | 481 | 550 | 15.2 | bdl | bdl | 0.33 | 15.472 | 30.801 | 0.6 | 11.116 | 85 | 899 | 7.1 | 1.568 | 3.68 |
| | **326** | **M19FLU25-28** | **TE-1** | **0** | **13.951** | **345** | **433** | **158.8** | **391.3** | **bdl** | **0.13** | **42.660** | **0.014** | **12.0** | **22.327** | **71** | **725** | **3.7** | **10.061** | |
| 2018 | 51.6 | M18FLU35 | TE-3 | 44.730 | 0.084 | 447 | 543 | 1.3 | 0.0 | 0.01 | 0.02 | 11.153 | 28.248 | 0.2 | 9.784 | 117 | 484 | 7.2 | 9.976 | 17.32 |
| | 51.6 | M18FLU36 | TE-3 | 45.985 | 0.523 | 444 | 505 | 8.4 | 0.1 | bdl | 0.10 | 12.087 | 25.654 | 0.4 | 10.002 | 118 | 449 | 6.3 | 0.180 | 15.00 |
| | 54 | M18FLU33 | TE-5 | 45.262 | 0.653 | 442 | 539 | 25.3 | bdl | 0.27 | bdl | 15.519 | 30.759 | 1.0 | 10.016 | 140 | 481 | 7.0 | 5.700 | 16.34 |
| | 54 | M18FLU34 | TE-5 | 44.749 | 0.675 | 452 | 529 | 27.8 | 0.1 | 0.16 | 0.34 | 15.680 | 30.505 | 1.0 | 9.822 | 140 | 473 | 7.0 | 1.012 | 17.29 |
| | **323** | **M18FLU1-4** | **TE-1** | **0** | **14.553** | **337** | **398** | **233.6** | **478.4** | **bdl** | **0.30** | **39.083** | **1.471** | **10.7** | **18.671** | **66** | **635** | **3.9** | **0.705** | |
| 2017 | 55 | M17FLU58 | TE-3 | 48.396 | 0.738 | 491 | 527 | 10.2 | bdl | bdl | bdl | 11.963 | 26.352 | nd | 10.982 | 63 | 474 | 6.2 | nd | 10.54 |
| | 46 | M17FLU57 | TE-5 | 49.482 | 0.598 | 493 | 545 | 19.2 | bdl | bdl | bdl | 13.732 | 30.015 | nd | 10.491 | 69 | 492 | 7.2 | nd | 8.54 |
| | **320** | **M17FLU49-52** | **TE-1** | **0** | **15.366** | **369** | **427** | **268.7** | **599.1** | **bdl** | **bdl** | **37.505** | **0.104** | **18.9** | **19.252** | **77** | **645** | **3.6** | **nd** | |
| **WC** | | | | | | | | | | | | | | | | | | | | |
| 2019 | 68 | M19FLU61[a] | WC-2 | 49.082 | 0.915 | 480 | 546 | 16.3 | bdl | bdl | bdl | 14.692 | 26.714 | 1.4 | 11.879 | 81 | 904 | 6.0 | 2.641 | 9.28 |
| | 68 | M19FLU62[a] | WC-2 | 48.703 | 0.430 | 446 | 561 | 7.9 | bdl | bdl | bdl | 11.976 | 28.296 | 0.7 | 10.664 | 81 | 928 | 6.2 | 1.203 | 9.98 |
| | 40 | M19FLU63[a,b] | WC-3 | 46.421 | 0.072 | 451 | 547 | 0.8 | 0.02 | 0.212 | 0.2 | 11.451 | 28.259 | 0.2 | 10.539 | 78 | 903 | 7.0 | 0.411 | 14.20 |
| | 40 | M19FLU64[b] | WC-3 | 49.276 | 0.148 | 449 | 546 | 2.1 | 0.1 | 0.204 | 0.4 | 11.211 | 28.160 | 0.6 | 10.581 | 77 | 893 | 6.6 | 0.411 | 8.92 |
| | **306** | **M19FLU09-12** | **WC-1** | **0** | **16.468** | **377** | **501** | **217.2** | **243.9** | **bdl** | **bdl** | **42.785** | **2.383** | **9.4** | **24.114** | **95** | **796** | **3.4** | **15.066** | |
| 2018 | 40 | M18FLU53 | WC-2 | 36.714 | 2.853 | 435 | 516 | 89.2 | 78.7 | bdl | 0.2 | 15.846 | 22.599 | 2.5 | 11.750 | 196 | 475 | 5.4 | nd | 32.14 |
| | 40 | M18FLU54 | WC-2 | 36.258 | 3.089 | 436 | 519 | 91.9 | 80.7 | bdl | 0.1 | 16.396 | 22.394 | 2.1 | 11.949 | 185 | 475 | 5.4 | 0.017 | 32.98 |
| | 35 | M18FLU55 | WC-3 | 42.802 | 0.930 | 457 | 519 | 27.1 | 0.3 | bdl | bdl | 12.736 | 25.613 | 2.4 | 10.619 | 179 | 471 | 6.2 | 0.071 | 20.88 |
| | 35 | M18FLU56 | WC-3 | 40.986 | 1.716 | 445 | 513 | 50.6 | 8.9 | bdl | bdl | 14.439 | 23.899 | 2.6 | 11.359 | 154 | 462 | 5.9 | 0.208 | 24.24 |
| | **319** | **M18FLU17-20** | **WC-1** | **0** | **15.342** | **385** | **483** | **333.5** | **428.5** | **bdl** | **bdl** | **39.758** | **0.087** | **44.3** | **21.828** | **152** | **763** | **3.6** | **10.078** | |
| 2016 | 131 | M16FLU60 | WC-3 | 38.938 | 2.338 | 384 | 372 | 98.5 | 3.1 | 0.3 | 0.3 | 16.428 | 14.982 | 1.8 | 12.036 | 111 | 524 | 5.6 | 2.908 | 28.03 |
| | 40 | M16FLU61[b] | WC-3 | 52.451 | 1.010 | 403 | 295 | 19.3 | bdl | 0.1 | bdl | 12.121 | 15.940 | 0.6 | 9.940 | 102 | 387 | 6.3 | 3.209 | 3.05 |
| | 78 | M16FLU62[b] | WC-3 0 | 55.219 | 0.403 | 418 | 276 | 6.5 | bdl | 0.1 | bdl | 11.318 | 13.669 | 0.3 | 11.602 | 113 | 372 | 6.6 | 2.566 | 0− |
| | 67 | M16FLU63[b] | WC-3 | 54.072 | 0.363 | 410 | 383 | 5.9 | bdl | 0.8 | bdl | 11.213 | 18.728 | 0.3 | 9.087 | 90 | 526 | 6.8 | 3.446 | 0.05 |
| | **316** | **M16FLU13-16** | **WC-1** | **0** | **15.586** | **382** | **499** | **272.9** | **261.7** | **bdl** | **bdl** | **41.075** | **6.084** | **3.9** | **18.989** | **119** | **796** | **3.2** | **0.932** | |
| | | Seawater. Millero et al. (2008) | | 54.100 | 0.178 | 468 | 545 | 0 | 0 | 0.001 | 0.028 | 10.28 | 28.30 | 0.140 | 10.21 | 87 | 838 | | 0 | |

*Note.* *bdl*: below detection limit. *nd*: no data. 0−: negative value from P[%] (Mg) estimation. Bold values correspond to focused vent fluid (black smoker) compositions. [a]No bell during this sampling. [b]Samples collected not right at the temperature probe location but less than 2m away.

time of deployment and recovery, clock drift) are available on the EMSO-Azores data portal (Cannat, Fontaine, et al., 2018; Cannat, Wheeler, Fontaine, et al., 2020; Cannat et al., 2021a; Cannat et al., 2021b).

### 3.3.2. Seafloor Pressure

For 2016–2017 and 2018–2020, we used data from a SBE 53 Bottom Pressure Recorder (Seabird Scientific; accuracy 0.6 psia, resolution 0.0004 psia, sampling interval 2 min) deployed on a benchmark (Figure 2i) near the northwest shore of the fossil lava lake (Figure 1 and Table S1 in Supporting Information S1). For 2017–2018, we used data from a SBE 54 Tsunami Pressure Sensor (Seabird Scientific; accuracy 0.6 psia, resolution 0.0011 psia, sampling interval 15 min), a component of the EGIM (EMSO Generic Instrument Module) deployed near the TE site (Figure 1). Full data and metadata (sampling frequency, time of deployment and recovery, clock drift, etc…) are available for 2017–2018 and 2019–2020 on the EMSO-Azores data portal (Ballu et al., 2021; Sarradin et al., 2018).

### 3.3.3. Current Direction and Velocity

We used data from two TCM-3 bottom currentmeters (Lowell Instruments LLC) deployed within 200 m of the TE and WC sites, respectively (Figure 1 and Table S1 in Supporting Information S1). TCM-3 instruments are made of buoyant housing hosting the logger, a magnetometer and an accelerometer, tied to ballast (Figure 2j). Orientation and tilt are used to calculate current direction and velocity, based on factory calibration. Measurements were made in bursts of 15s spaced by 1 mn, with a sampling rate of 8 Hz during the burst. Full data and metadata (instrumental accuracies and resolutions, sampling frequency, time of deployment and recovery, clock drift, etc.) are available on the EMSO-Azores data portal (Cannat, Wheeler, et al., 2018; Cannat, Wheeler, Chen, et al., 2020; Cannat et al., 2017). For current velocities <5 cm.s$^{-1}$, uncertainties for the direction of the current are larger than the nominal accuracy of the magnetometer.

### 3.4. Processing of Times Series Data

After the recovery of the instruments, all time-series were plotted and visually checked for data gaps and outliers. A linear clock drift correction was applied. Spectral analysis was then performed using the multi-taper method (Thomson, 1982) with adaptive weighting (Percival & Walden, 1993) used in previous studies of tidal forcing effects on venting temperatures at Lucky Strike (Barreyre & Sohn, 2016; Barreyre et al., 2014a). We derived the time variability of the power spectral density (PSD) and the coherence and phase lag between fluid temperature, seawater pressure head and bottom current velocity at the semi-diurnal M2 frequency. We used a sliding time window of 30 days, with a 1 day sliding time (bandwidth product of NW = 4; Thomson, 1982). Tests with both longer and shorter sliding windows are shown in Figure S2 of the Supporting Information S1. Phase lag estimates are reported only for time periods with coherence >0.75.

## 4. Local Geology and Monitoring Locations at the Tour Eiffel and White Castle Hydrothermal Sites

Both Tour Eiffel (TE) and White Castle (WC) comprise a sulfide mound with several focused vents (Figures 2a and 2f), a wider domain of sulfide deposits and of volcaniclastic deposits that have been indurated by hydrothermal precipitates (Figures 3a, 3b, and 3e) and an outer domain of non-indurated to slightly indurated volcaniclastic deposits (Figures 3b–3d). These deposits are up to 1.5 m-thick at the TE and WC sites, rest unconformably on brecciated basalts (Figures 3c and 3e) and are commonly degraded into a sandy material (Figure 3b). The indurated volcaniclastic deposits have been referred to as the "slab formation" (Fouquet et al., 1994). They are made of clasts of basalt, basalt glass, plagioclase phenocrysts, barite and sulfur grains, cemented by amorphous silica and barite (Costa, 2014; Fouquet et al., 1994; Langmuir et al., 1997). The slab acts as a cap through which fluids can only discharge via cracks (Figures 3a and 3e; Cooper et al., 2000), some of which form flanges (Figure 3a). Cracks in the slab and in the non-indurated volcaniclastic are commonly associated with local tilting and swelling or collapse of the seafloor, which we infer are due to anhydrite precipitation and/or dissolution in the shallow substratum, as proposed for the TAG hydrothermal field (Humphris et al., 1995).

Tour Eiffel (Figure 4a) is one of the largest LSHF sites. It is located on top of a N to NNW-trending 2–24 m-high east-facing fault scarp and has a ~15 m-high sulfide mound (Figure 4c) with several black smokers (one of which was monitored at location TE-1; Figure 2a). The outer limits of the TE site, defined so as to enclose all
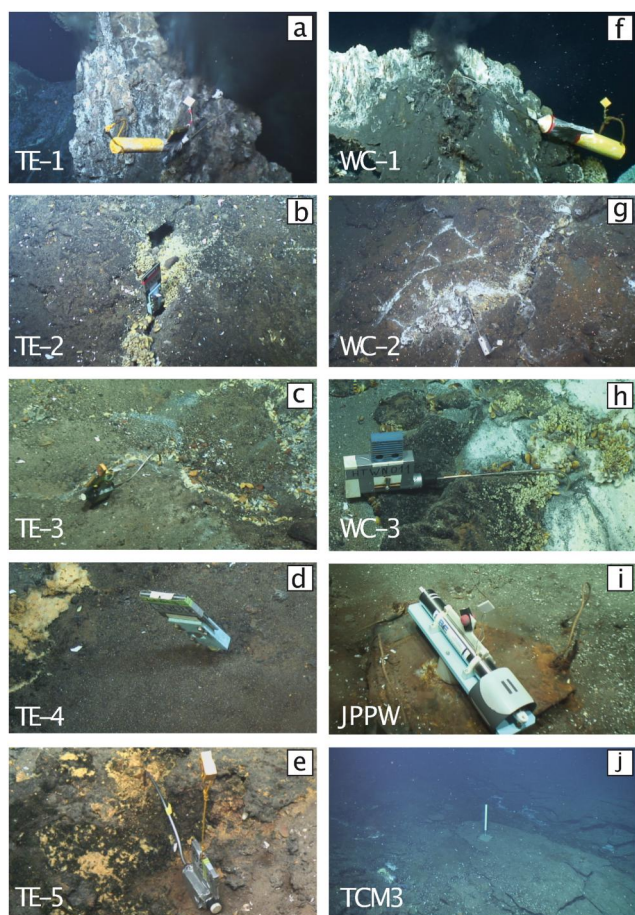
**Figure 2.** ROV video snapshots showing examples of the temperature probes, seafloor pressure probes and currentmeters deployed as part of the monitoring experiment (locations in Figures 1 and 4). (a) High-temperature WHOI (HTW) probe deployed in 2017 at a Tour Eiffel focused vent (monitoring location TE-1). (b) Low-temperature WHOI (LTW) probe deployed in 2017 in a Tour Eiffel venting crack (monitoring location TE-2); note bacterial mats and mussel assemblage. (c) High-temperature NKE (HTNKE) probe deployed in 2018 in a mussel-lined Tour Eiffel venting crack in non-indurated volcaniclastic formation (monitoring location TE-3). (d) LTW probe deployed in 2017 at Tour Eiffel in brownish sandy area next to yellow iron-oxidizing bacterial mats (monitoring location TE-4). (e) LTW probe deployed in 2018 at Tour Eiffel in vent nested in yellow iron-oxidizing bacterial mats (monitoring location TE-5). (f) HTW probe deployed in 2017 at a White Castle focused vent (monitoring location WC-1). (g) HTNKE probe deployed in 2016 at White Castle in crack in slab formation (monitoring location WC-2). (h) New high-temperature WHOI (HTWN) probe deployed in 2017 at White Castle in sandy area next to mussel-bearing slab panel (monitoring location WC-3); note white sulfate precipitates and bacterial mats in diffuse venting area. (i) SBE53 pressure probe deployed in 2018 at the JPPW benchmark. (j) TCM3 currentmeter deployed in 2016 on non-indurated layered volcaniclastics to the south of Tour Eiffel. Details on these probes in Table S1 of the Supporting Information S1.

nearby active diffuse venting areas, extend up to 90 m along the fault scarp (Figure 4a). The TE sulfide tower is set in a 35 m long by 25 m-wide elliptical domain of indurated slab with small sulfide chimneys, venting cracks (such as the crack monitored at location TE-2; Figures 2b, 3a, and 5a) and flanges (such as near the TEMPO ecological module; Sarrazin et al., 2007; Figure 5a), feeding mussels, arthropods, echinoderms, crustaceans (Cuvelier et al., 2009; Dover et al., 1996; Girard et al., 2020) and microbial mats (Crépeau et al., 2011; Sarradin et al., 1999).

White Castle (Figure 4b) is a smaller site set in a ∼30 m long elliptical volcanic depression in the extensively fissured northern slopes of the southern cone-shaped volcano, only 50 m to the south of the fossil lava lake (Figures 1 and 4d). The ∼3 m-high WC sulfide mound (Figures 2f and 5b) with several black smokers (monitoring location WC-1; Figure 2f) is on the southern rim of the elliptical depression (Figure 4b). As at TE, diffuse fluids at WC discharge in mussel-lined cracks and flanges in the sulfide mound and in centimeter to decimeter-wide cracks in the indurated slab (monitoring location WC-2; Figure 2g). Several such cracks connect to the sulfide mound (Figure 5b) and locally develop decimeter-high sulfide chimneys (Figure 2g) that vent clear shimmering fluid. We observed northward growth of the WC sulfide mound by ∼2 m in 2016–2017, progressing over the fissured slab (Figure 5b). We had to move monitoring location WC-2 northward in 2017 because its 2016 location had become part of the sulfide mound.

The indurated slab domain at WC extends downslope to the north to the bottom of the depression (Figures 3e and 4b). This slab is fractured and forms isolated panels, 1–3 m wide, particularly in the lower slopes. These panels rest on a gray sandy substrate made of disaggregated volcaniclastic deposits with variable proportions of sulfide and sulfate-bearing minerals. At TE, similar yet less extensive domains of gray sandy substrate are found along the outer limits of the slab (Figures 3a, 3b, and 5a) and line cracks in the non-indurated layered volcaniclastites (monitoring location TE-3; Figure 2c). These gray sandy substrate domains had not been described prior to this study, probably because they are not visible in the black and white photomosaics of the vent field analyzed by Barreyre et al. (2012). They vent slowly oozing fluids and host polychetes, gastropods and isolated small mussels (monitoring location WC-3; Figure 2h). They are locally capped by mm-thick white sulfate precipitates (such as at monitoring location WC-3; Figure 2h) or by microbial mats (Sarrazin et al., 2009), forming the white diffuse venting patches mapped by Barreyre et al. (2012). They pass laterally, at both WC and TE, to brownish sandy domains that display no visual evidence of fluid venting (monitoring location TE-4; Figures 2d and 5a). In these brownish domains, there are also networks of sinuous patches with yellowish iron oxidizing bulbous microbial mats (Astorch-Cardona et al., 2023). These yellowish patches are well developed at TE (Figures 2d, 2e, and 5a). They are also found in a set of radial cracks in the north of WC (Figures 3d and 4b). Monitoring location TE-5, in the non-indurated volcaniclastic deposits north of the TE sulfide mound (Figures 2e and 4a), stands out with shimmering waters indicative of relatively fast venting velocities. The other observed yellowish patches do not show visual evidence for fluid venting, yet the microbial mats suggest that hydrothermal fluids do indeed ooze out, at least episodically.
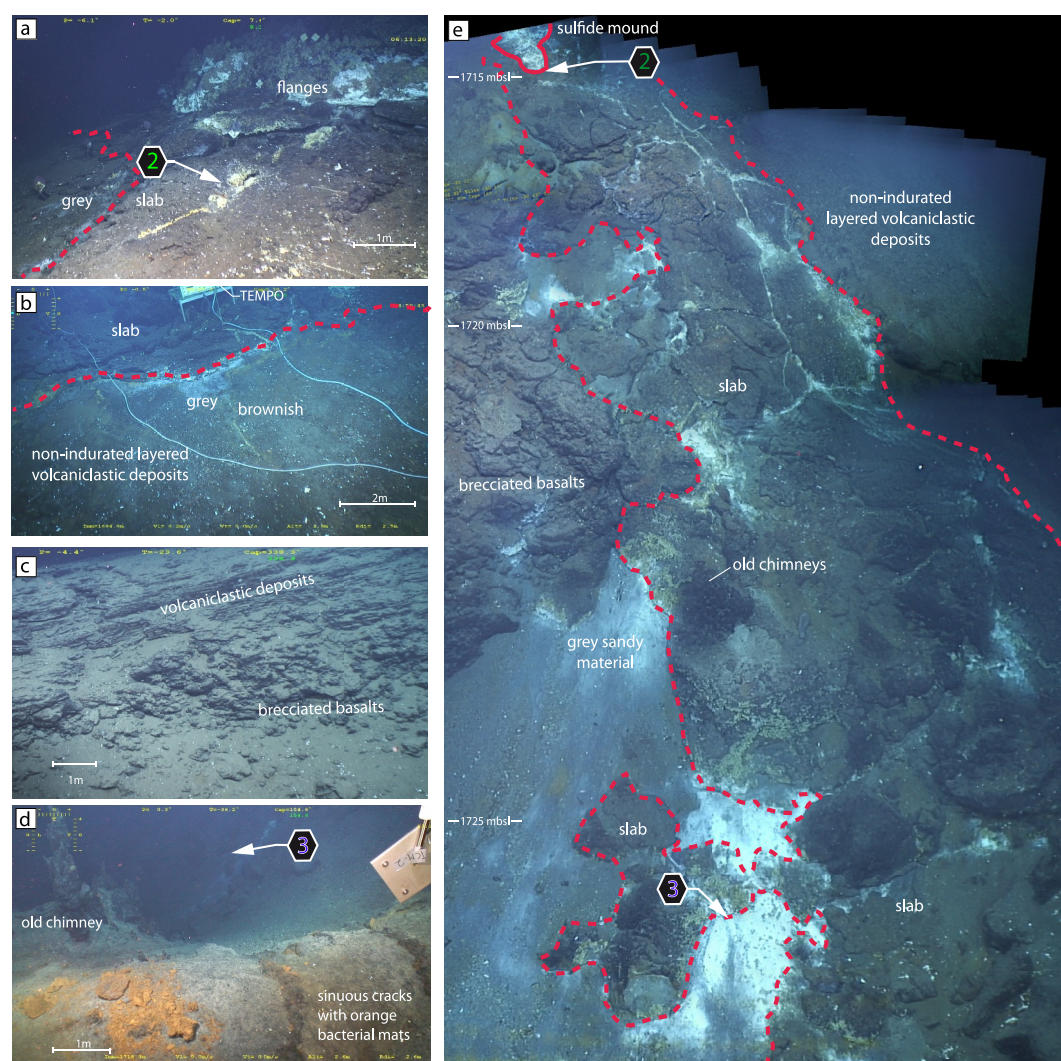
**Figure 3.** ROV video snapshots at and near the Tour Eiffel (TE) and White Castle (WC) sites. These snapshots are located in Figures 4a and 4c. Hexagons with numbers refer to monitoring locations. Scales are indicative. (a) View to NNE over monitoring location TE-2 (mussel-lined venting crack in slab), note small sulfide mound in background with white sulfate deposits and bacterial mats; red dashed line is limit to non-indurated volcaniclastic formation, as in Figure 4b; gray is gray sandy material as in (b) and (e). (b) View to the north showing the ecological module TEMPO (and connecting cables) at the southern edge of the slab (red dashed line) at TE, with non-indurated volcaniclastic deposits in the foreground. (c) View to the west over a minor fault scarp exposing the brecciated basalt basement of the TE site, with layered volcaniclastic deposits on top. (d) View to the south over the edge of the WC depression, fissures lined with brown-yellow bacterial mats in sandy volcaniclastic formation. (e) View to the south over monitoring locations WC-2 and WC-3, photomosaic of ROV video snapshots covering depths of 1,713–1,727 mbsl. Red line is the limit of WC sulfide mound and red dashed line is the limit of indurated volcanoclastic slab with small extinct sulfide chimneys, as in Figure 4d. Note brecciated basalt basement to the left, non-indurated layered volcaniclastic deposits on the right, a network of venting fissures lined by mussels and white bacterial mats in slab and gray to brown sandy material with patches of white sulfate precipitates in the lower slopes.

## 5. Time Series of Focused and Diffuse Fluid Chemistry at the Tour Eiffel and White Castle Vent Sites

The chemistry and sampling temperature of focused and diffuse fluids sampled between 2016 and 2019 at the TE and WC monitoring sites are presented in Table 1. Hydrothermal endmember fluids (temperatures > 306°C) have low pH ($\leq$4.5) and are depleted in Na and Cl and enriched in $H_2S$, Si, Ca, Ba, Fe, Cu, and Zn compared to seawater. Chlorinity is consistently lower at TE (Cl < 433 mmol/L; Na <369 mmol/L) than at WC (Cl up to 501 mmol/L in 2019), consistent with previous observations of lower Cl concentration at the southeastern Lucky
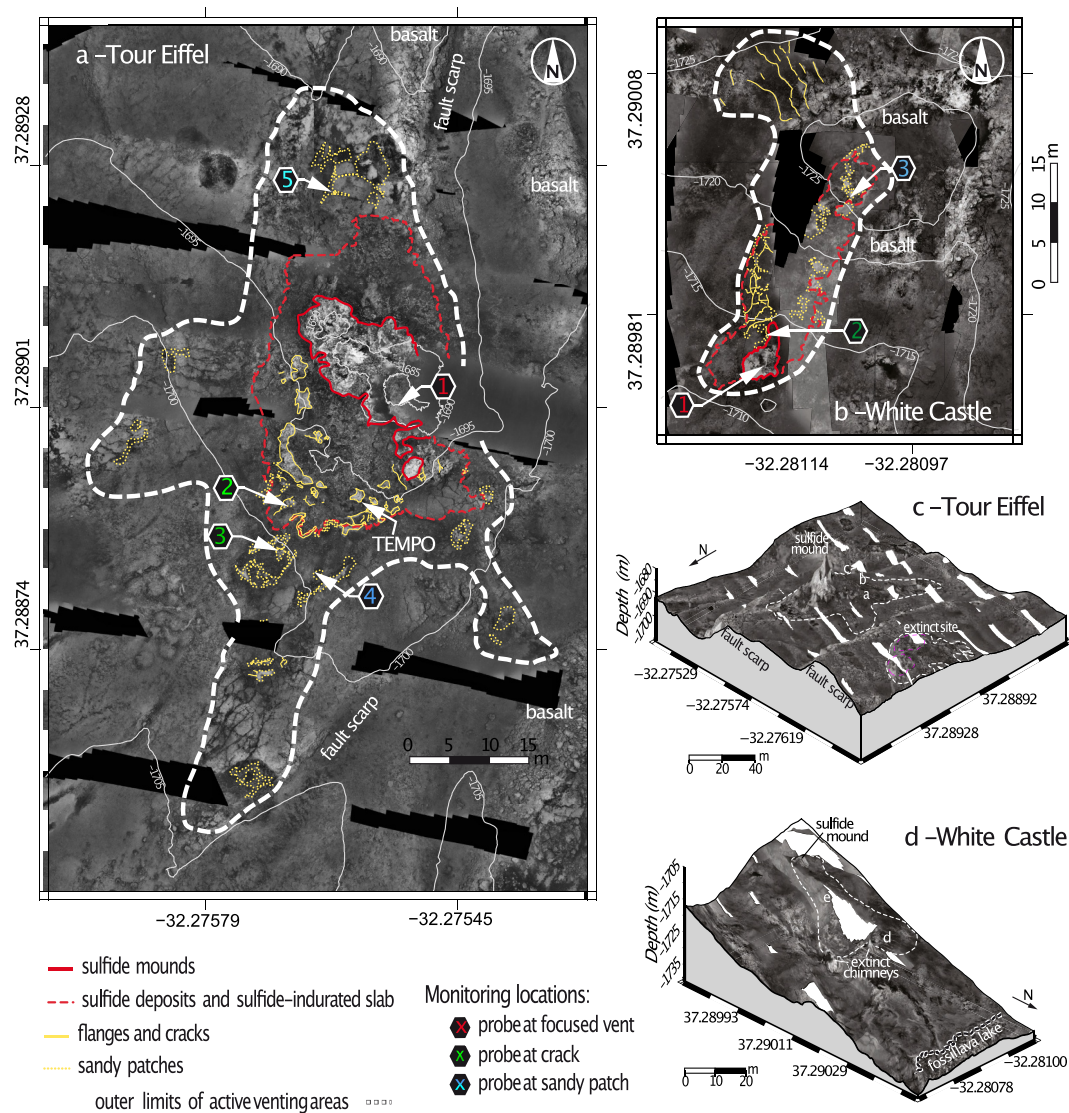
**Figure 4.** Geological setting of the Tour Eiffel and White Castle hydrothermal sites. (a) and (b) Map views with temperature monitoring locations shown by numbers in hexagons: red for focused vents, green for diffuse venting cracks and blue for diffuse venting sandy patches (for TE site, venting areas modified from Barreyre et al. (2012)). TEMPO in (b) is an ecological monitoring module. In these maps, TE and WC are shown on the same scale. White dashed line is outer contour of each site; (c) and (d) 3D views of photomosaic draped over HR bathymetry; (c) 3D view of photomosaic at the Tour Eiffel site; (a–c) letters refer to location of ROV video snapshots in Figure 3; dashed white line is outer contour of the active TE site and of an extinct site to the west, with two elliptical depressions (dashed pink lines in 4c) interpreted as collapsed areas after anhydrite dissolution; (d) 3D view of photomosaic at the WC site; (d and e) letters refers to location of ROV video snapshot in Figure 3; dashed white line is outer contour of active WC venting; double dashed white line in the north is the outer limit of the fossil lava lake.

Strike sites (Chavagnac et al., 2018; Langmuir et al., 1997; Von Damm et al., 1998). Other major cations like Ca and K have similar concentrations at the two sites, while in any given year, Mn is more abundant in WC end-member fluids and Fe more abundant at TE. Strontium is consistently more abundant at WC (up to 151 µmol/L). Overall, the endmember fluid compositions in Table 1 are similar to the concentrations measured in fluids sampled at the two sites since 2010 (Chavagnac et al., 2018). We use these hydrothermal endmember fluids as a reference to study the temporal chemical evolution of diffuse fluids.

Diffuse fluid temperatures, measured just before sampling, range between 35 and 131°C (Table 1) and the fluids pH range between 5.42 and 7.22 (near seawater value). The most acidic values correspond to fluids sampled in
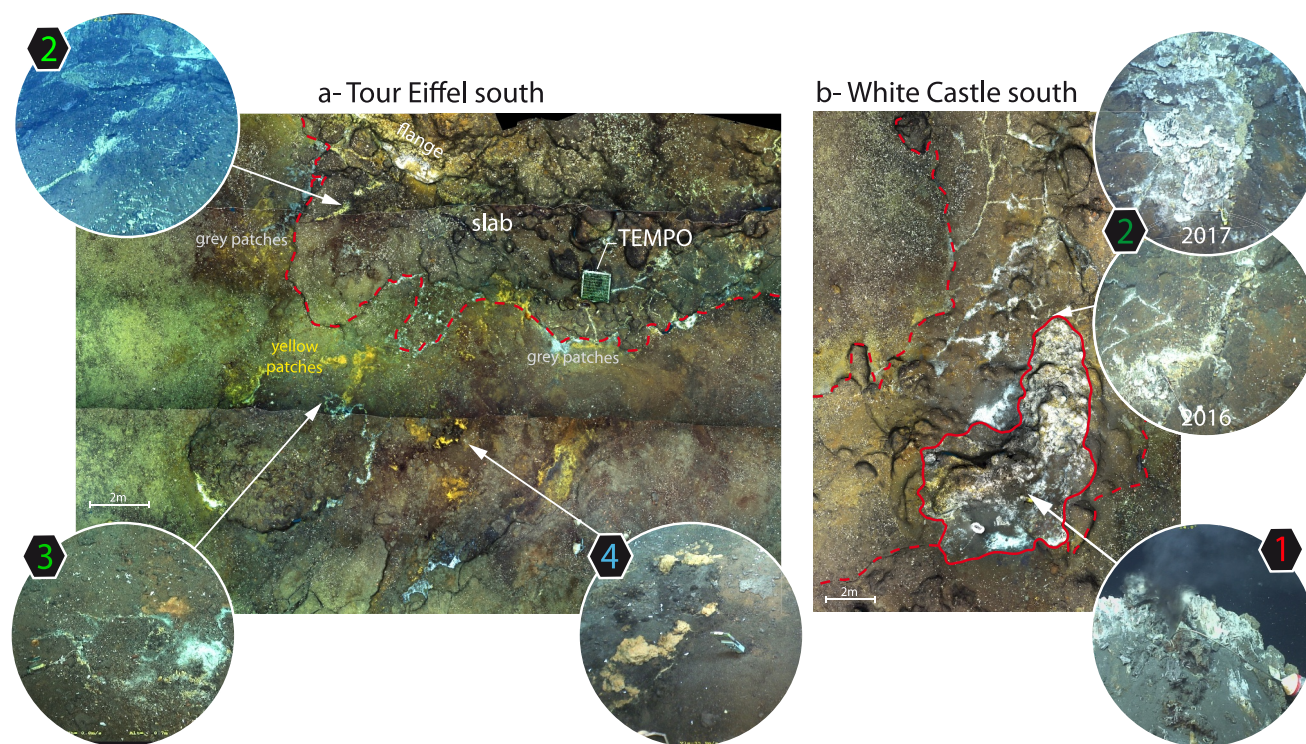
**Figure 5.** High-resolution OTUS photomosaics (acquired in 2018) of the Tour Eiffel and White Castle sites, with ROV video snapshots of monitoring locations TE-2, TE-3, TE-4, WC-1, and WC-2. Red lines (dashed and plain) as in legend for Figures 4a and 4b. (a) South TE, note white precipitates and bacterial mats on volcaniclastic deposits north of TE-2 mussel-lined crack, square frame of the TEMPO ecological module, an array of fine mussel-lined cracks at TE-3, yellow bacterial mats just west of TE-4 and corresponding orange patches in the OTUS photomosaic. (b) South WC, note black smoker at WC-1, location of WC-2 in crack near the base of WC sulfide mound, with northward growth of this mound between the 2016 and 2017 probe deployments (WC-2 snapshots look south over the same area).

2016 at monitoring location WC-3 (diffuse patch in gray sandy material; Figure 2h) and in 2018 at monitoring location WC-2 (crack in the slab within 1 m of the edge of the sulfide mound; Figure 2g). Mg concentrations vary between 36.2 mmol/L (WC-2 crack in 2018; Table 1) and 55.2 mmol/L (diffuse venting patch near WC-3 in 2016; Table 1), close to the seawater concentration. Chlorinity increases with Mg concentrations in most samples, consistent with predicted conservative mixing trends between seawater and endmember fluids (Figure 6a and Figure S3 in Supporting Information S1). Samples collected in 2016 at WC-3 plot well below these trends at very low chlorinity (Figure 6a). Na concentrations are also lower in these samples (Table 1). Higher Mg concentrations were measured at all sampling sites in 2019 compared to previous years and particularly to 2018: while it might be a real signal, there is a possibility that sampling performed in 2019 with the manned submersible Nautile incorporated a greater proportion of entrained seawater because it was more difficult to visually control near seafloor sampling operations from the higher standpoint of the Nautile.

Si concentrations range between 0.07 and 3.08 mmol/L (Table 1). The highest values were measured for the WC-2 crack in 2018. Si concentrations tend to decrease with increasing Mg, as expected for an increasing dilution of the endmember fluid with seawater (Seyfried & Bischoff, 1977), but three groups of samples can be identified. Group 1 (gray field in Figure 6b) has low Mg concentrations and Si concentrations that are consistent or higher than those predicted for conservative mixing of seawater and endmember fluids. It includes the TE-3 and TE-5 2019 samples and three of the low chlorinity WC-3 2016 samples. Group 2 (light red field in Figure 6b) has lower Mg concentrations (48–49.5 mmol/L) and Si concentrations lower than predicted for conservative mixing of seawater and endmember fluids. Group 3 (light blue field in Figure 6b) has even lower Mg concentrations (36–46 mmol/L) and Si concentrations lower by about 1.5 mmol/L than predicted by conservative mixing trends at these Mg concentrations. The lowest Mg and highest Si concentrations for group 3 (36.25 and 3.09 mmol/L respectively; Table 1) were measured in the WC-2 2018 samples.

Mn concentrations in diffuse WC fluids (Table 1 and Figure S4 in Supporting Information S1) range between 0.8 and 91.9 μmol/L and Mn concentrations tend to decrease at increasing Mg, as expected for an increasing dilution of the endmember fluid with seawater, but the 3 groups identified in Figure 6b are also distinct. Magnesium, silica and manganese have all been used as chemical tracers to evaluate the proportion of hydrothermal end-member fluids in MOR diffuse effluents (Butterfield et al., 2004; Field & Sherrell, 2000; Hawkes et al., 2013; Von Damm et al., 1985; Waeles et al., 2017). Silica and Mn cannot, however, be considered as conservative tracers in the samples studied here based on the Si and Mn versus Mg trends (Figure 6b and Figure S4 in Supporting Information S1). We therefore use Mg as the least unreliable dilution tracer to estimate the contribution (%E) of hydrothermal endmember fluids to diffuse venting at the TE and WC monitoring locations (Table 1). %E values range between 0% for TE-3 in 2019 and WC-3 in 2016 and 33% for WC-2 in 2018. Note that even for low %E values, $H_2S$ contents can be significant and are variable at a given sampling location (Table 1).

K (9.0–12.0 mmol/L) and Ca (11.1–16.4 mmol/L) concentrations in diffuse fluids (Table 1) are similar or higher than seawater values and the three groups of samples defined in the Si or Mn versus Mg graphs (Figure 6b and Figure S4 in Supporting Information S1) are also visible in K versus Mg (Figure 6c) and Ca versus Mg graphs (Figure 6d). Group 3 samples define a rough trend that is offset to lower K and Ca concentrations by 1–2 mmol/L relative to predicted seawater-endmember fluid conservative mixing lines. Fluids sampled at TE-5 in 2018, however, that belong to Group 3 based on Si and K concentrations, plot on the seawater-end-member fluid conservative mixing line with respect to Ca (Figure 6d). Group 2 samples also tend to plot near these conservative mixing lines for both K and Ca. Group 1 samples have scattered K concentrations and Ca concentrations above the conservative mixing lines (Figure 6d).

$SO_4$ concentrations in diffuse fluid range between 13.66 mmol/L in one of the WC-3 2016 chlorine-depleted samples and 30.8 mmol/L at TE-5 in 2019 (Table 1). Figure 6e shows total $SO_4$ relative to Ca concentration and the linear trends that would correspond to conservative mixing of seawater with hydrothermal endmember fluids (Figure S3 in Supporting Information S1). With the exception of the chlorine-poor 2016 WC-3 samples, diffuse fluid plot either on or above these conservative mixing lines, in a domain that would correspond to anhydrite dissolution. All TE-5 sample plot in this dissolution domain, which could explain their relatively high Ca concentrations (Figure 6d). Fluids sampled at the TE-3 crack plot near the conservative mixing lines in 2017 and 2018 and in the anhydrite dissolution domain in 2019 (Figures 6e and 6f). Fluids sampled at the WC-2 crack plot near the mixing line in 2018 and then into anhydrite dissolution in 2019. The low chlorinity fluids collected at WC-3 in 2016 plot in the anhydrite precipitation domain. Fluids from the same location (Figure 2h and Figure S1c in Supporting Information S1) plot on the mixing line in 2018 and into the anhydrite dissolution domain in 2019 (Figures 6e and 6f). Ba concentrations (0.2–2.5 μmol/L; Table 1) are higher than seawater values (Millero et al., 2008), with the highest concentrations measured in 2018 at WC-2 and WC-3 (Table 1). All samples, except for the low chlorinity fluids collected at WC-3 in 2016, plot near the conservative mixing trends in the $SO_4$ versus Ba concentrations diagram (Figure S4b in Supporting Information S1). Ba concentrations are 3 orders of magnitude lower than Ca concentrations in all samples, suggesting that while some of the variability observed in $SO_4$ concentrations may result from barite ($BaSO_4$) precipitation, it likely plays a minor role, compared to anhydrite precipitation.

In Figure 6g, we plot the Mg concentration of diffuse fluids against fluid temperatures measured during sampling at monitoring locations TE-2, TE-3 and TE-5 and WC-2 and WC-3. If Mg is indeed an indicator of the degree of hydrothermal endmember fluid dilution by seawater (Table 1), lines drawn from the Mg concentration and temperature of seawater, to those of black smoker fluids (Figure S3f in Supporting Information S1) would correspond to mixing with no conductive heat gain or loss. While the 2018 TE-3 and TE-5 samples do plot on these lines (Figure 6g), the other samples plot either below (WC-2 2018) suggesting conductive cooling of the endmember fluid or of the mixed fluid prior to venting or above these lines (WC-3 2016, WC-2 2019, TE-3 and TE-5 in 2017 and TE-5 2019), suggesting conductive heating of the seawater or of the mixed fluid prior to venting. Figure 6g also shows the range of temperatures measured by in situ autonomous probes at each fluid venting location during 1 week before and 1 week after fluid sampling. With the exception of WC-2 2019, these recorded temperatures are consistent with those measured during sampling operations, indicating that the collected samples adequately represent fluids that discharge at each monitored location. Temperatures recorded by the in situ autonomous temperature probes in 2019 at WC-2 were >180°C, significantly higher than the sampling temperatures at this site for the same year (Figure 6g). This discrepancy is most likely due to the large variations of venting fluxes documented in dive videos at scales of a few centimeters along the WC-2 crack.
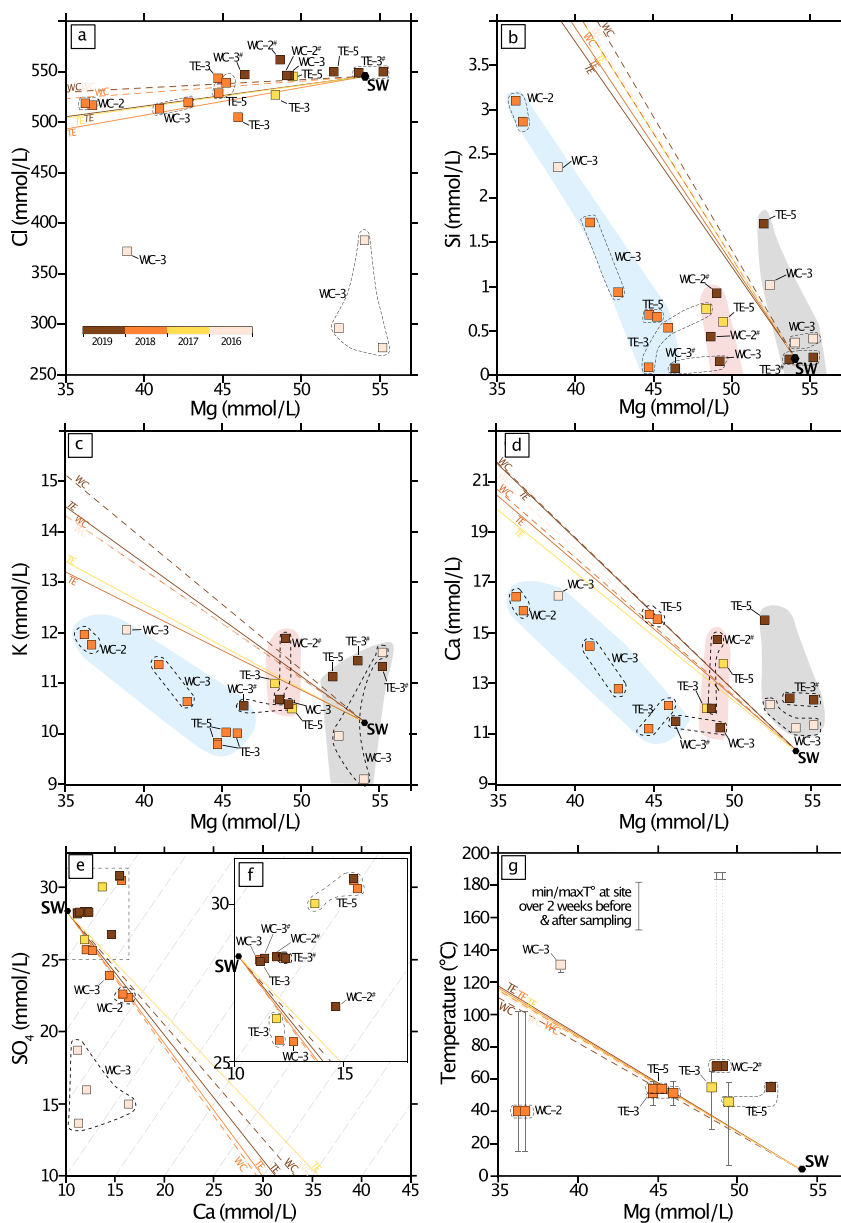
**Figure 6.** Chemical diversity of diffuse fluids sampled at Tour Eiffel (TE) and White Castle (WC) monitoring locations TE-3, TE-5, WC-2, and WC-3 in 2016, 2017, 2018, and 2019 (Table 1 and Figure S1 in Supporting Information S1). Solid and dotted lines labeled WC or TE joins the end-member black smoker fluid compositions sampled at monitoring locations TE-1 and WC-1 (Table 1 and Figure S3 in Supporting Information S1), to seawater composition (SW) from Millero et al. (2008). (a) Magnesium and chloride contents. Except for fluids sampled near WC-3 in 2016, data plot near the end-member fluid to SW lines. (b) Magnesium and silicon contents. Three groups of samples are identifiable based on their Mg content and position with respect to the end-member fluid to SW lines (group 1 in gray, group 2 in pink, group 3 in blue). Group 3, with the highest Mg concentrations defines a trend parallel to the end-member fluid to SW lines but offset to lower Si contents (c) Magnesium and potassium contents and (d) Magnesium and calcium contents. The three groups identified in (b) are also shown. (e) Calcium and sulfate ion contents. Gray dashed lines show the trends expected for anhydrite dissolution or precipitation. Fluids sampled near WC-3 in 2016 are again outliers. Other samples plot near or above (suggesting anhydrite dissolution in the substratum) the end-member fluid to SW lines. (f) Magnesium content and temperature of the diffuse fluids. Only samples collected within 1 m from autonomous temperature probe locations (Table 1) are shown. Solid and dotted lines labeled WC or TE joins the Mg content of black smoker end-member fluids and their temperature measured by the ROV or Nautile prior to fluid sampling, to seawater Mg content (Millero et al., 2008) and temperature (SW). Gray bars show the min and max temperature measured by autonomous temperature probes over a week before and after fluid sampling.

## 6. Temporal Variability of Vent Fluids Temperature at the Tour Eiffel and White Castle Sites

The fluid temperatures measured between September 2016 and July 2019 at the TE and WC monitoring locations are presented in Figure 7 (and Figure S7 in Supporting Information S1). The two monitored black smoker vents (TE-1 and WC-1; Figures 2a and 2f) are our reference for the end-member fluid upflow at both sites. Their temperature mostly ranges between 295 and 329°C, with occasional drops (Figure 7a), interpreted as due to local hydraulic perturbations in the sulfide edifices (Barreyre et al., 2014a). A steady and slow temperature decrease, from 306°C down to 260°C, in June–August 2019 at TE-1 is also probably due to local clogging of the vent conduit. Aside from these occasional events, hydrothermal endmember fluid temperatures display periodic or semi-periodic variations of a few tens of °C to a few °C (Figures 7b and 7c), similar to those reported for earlier years of monitoring at LSHF vents (Barreyre & Sohn, 2016; Barreyre et al., 2014b). The Power Spectrum Density (PSD) energy at semi-diurnal tidal frequencies (N2, M2, S2, K2) is low overall at the TE-1 vent and higher at the WC-1 vent, particularly in 2016–2017 (Figures 8a and 8b). The coherence at the semi-diurnal M2 frequency between hydrothermal endmember fluid temperatures at TE-1 and WC-1 and seafloor pressure (CM2) varies between 0 and 0.75 at TE-1 and between 0 and 0.95 at WC-1 (Figure 7d). CM2 values vary over timescales of a fortnight to a few months and phase lags for periods of higher CM2 range between 177° and 231° (Figure 7e), with smooth variations over 1.5–2.5 months at WC-1 in 2018–2019. All of these characteristics are comparable to those reported for pre-2015 Lucky Strike black smoker temperatures by Barreyre et al. (2014b) and Barreyre and Sohn (2016).

### 6.1. Diffuse Fluid Temperatures at Monitored Venting Cracks and Patches

Temperatures recorded at the monitored venting cracks span a broader range (from 7°C at TE-2 to 307°C at WC-2; Figure 7f) than those recorded at patches (from 35°C at TE-4 to 160°C at WC-3; Figure 7i). Temperatures at venting patch WC-3 (125°–160°C; Figure 7i) increased throughout the year in 2016–2017 and 2017–2018, then decreased in 2018–2019; temperatures measured in 2017–2019 in brownish sandy material at TE-4 (Figure 2d), with no visible evidence for fluid venting, varied between 35 and 39°C over periods of ~140 days (Figure 7i); and temperatures at TE-5 (Figure 2e) have been stable (55°–58°C) over the 3 years of recording (Figure 7i). The probe fell out of TE-5 in late February 2018 and out of TE-4 in mid-February 2019, subsequently recording seabed temperatures (4.5–5.5°C; Figure 7i). Temperatures at venting cracks ranged between 7° and 18°C at location TE-2 (Figure 2b), 25° and 80°C at TE-3 (Figure 2c) and 18 and 307°C at WC-2 (Figure 2g). TE-3 probe fell off the crack and recorded seabed temperatures from early April 2019 onward (Figure 7f). Temperatures at TE-2 remained low (7–18°C) over the 3 years of the experiment, while temperatures at TE-3 varied between 25 and 80°C, over periods of a few days to several months (Figure 7f). Temperatures recorded at WC-2 in 2016–2017 are only 10–40°C lower than those recorded at the WC-1 focused vent ~4 m away (Figure 7a and Figure S7d in Supporting Information S1). From August 2017 onward, after the probe was moved 2 m to the north along the same crack following the growth of the sulfide mound (Figure 5b), temperatures at WC-2 were lower (around 200°C), then decreased from around 170°C in January 2018, to <50°C in March and ~20°C in August 2018. Temperatures at WC-2 increased again to ≥200°C following the August 2018 redeployment (Figure 7f).

The most visible difference between the temperature recorded at venting cracks and patches is that, at venting patches, semi-diurnal variations are small (a few tens of °C; Figure 9c), to absent (Figure 9d) and PSD signatures at the semi-diurnal tidal frequencies (N2, M2, S2, K2; Figures 8a and 8b) are weak, particularly at TE-5 (Figure 8a). Temperature variations >1°C at venting patches occur progressively over periods of several weeks to months (Figure 7i). By contrast, at venting cracks, episodic variations of several °C are frequent (Figure 7g). Semi-diurnal variations are also common and typically span a few °C (Figures 9a and 9b) and the corresponding PSD values are significant, particularly at WC-2 (Figures 8a and 8b). The lowest semi-diurnal PSD values for a venting crack were recorded at TE-3 in 2018–2019 (Figure 8a).

### 6.2. Coherence Between Diffuse Venting Fluid Temperatures and Seawater Pressure at the Semi-Diurnal M2 Frequency

At venting patches, the coherence between venting fluid temperatures and seawater pressure at the semi-diurnal M2 frequency (CM2) is mostly small (<0.75), particularly at TE-5 (Figure 7j). During intervals of significant CM2, the amplitude of semi-diurnal temperature variations is small (up to 0.8°C at WC-3; Figure 9d) and time
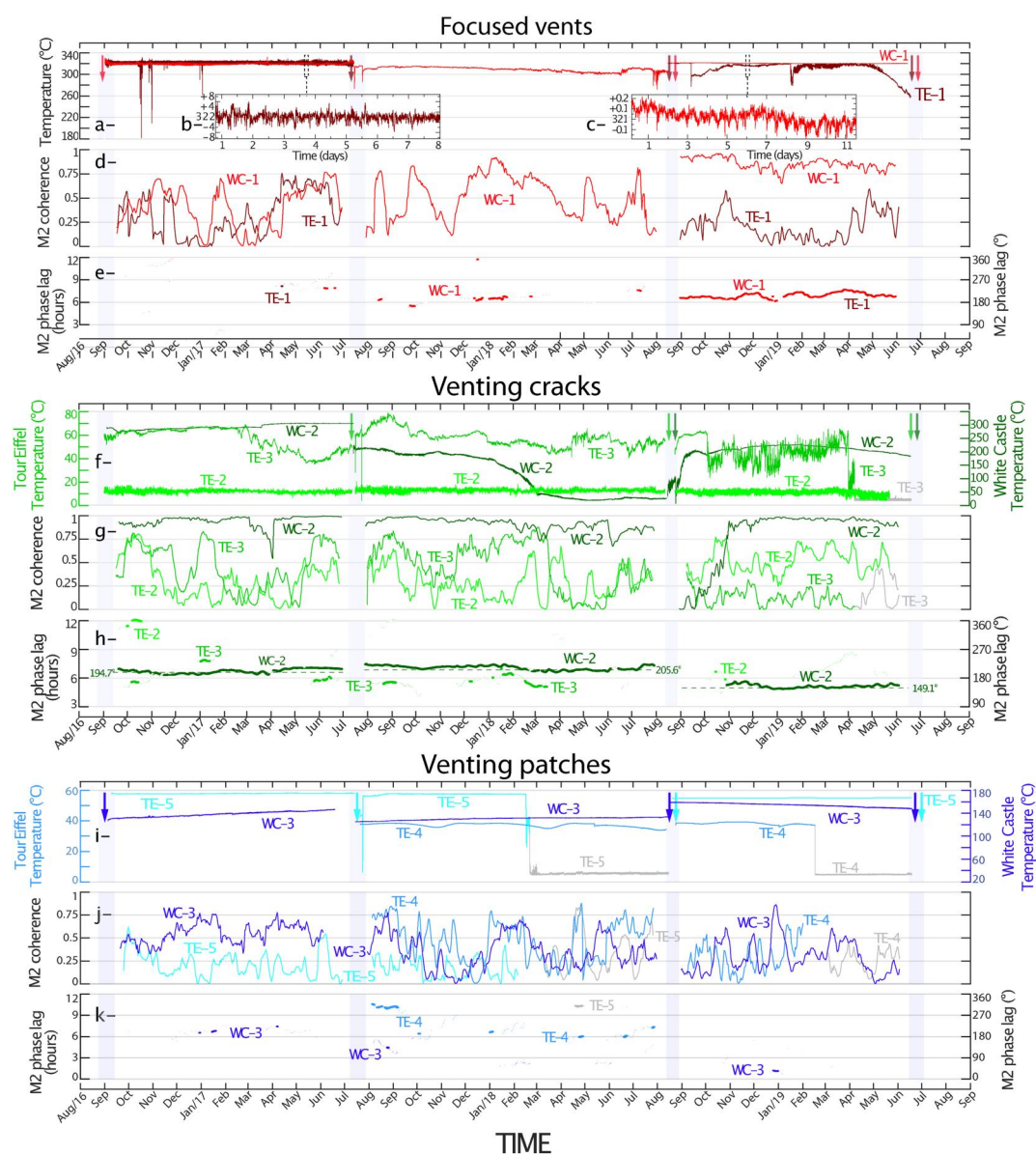
**Figure 7.** Venting temperatures recorded at Tour Eiffel and White Castle monitoring locations from August 2016 to July 2019. (a–e) Temperatures recorded at focused vents TE-1 (dark red) and WC-1 (light red). (f–h) Temperatures recorded at venting cracks TE-2 (light green), TE-3 (green) and WC-2 (dark green). (i–k) Temperatures recorded at venting patches TE-4 (pale blue), TE-5 (electric blue) and WC-3 (dark blue). Temperature records for periods when a probe had fell off the vent and recorded near seafloor seawater temperatures are shown in gray. Panels (b and c) show details of tidally modulated temperature variations at focused vents. The second full panel for each group of vents (d, g, and j) shows the time variation of the coherence between venting temperature and seafloor pressure at the M2 tidal frequency (30 days sliding window, 1 day sliding time). The third panel for each group of vents (e, h, and k) shows the time variation of the corresponding phase lag for M2 coherence values >0.75 (phase lags for M2 coherence >0.5 are also shown as thin lines). Light gray bands correspond to the duration of maintenance cruises and colored arrows show the sampling time for the fluids reported in Table 1.

periods with very low CM2 values at TE-4 and TE-5, for example, in December 2018 (Figure 7j), correspond to very stable temperatures (within the probes resolution; Figure 9c). Fortnightly CM2 maxima that coincide at WC-3 and TE-4 (e.g., in early October 2016, late September–early November 2017 and in late June 2018) correspond to spring tides (Figure S6 in Supporting Information S1). CM2 variations over longer timescales (up to several months) are distinct between venting patches and also between these patches and nearby venting cracks (Figures
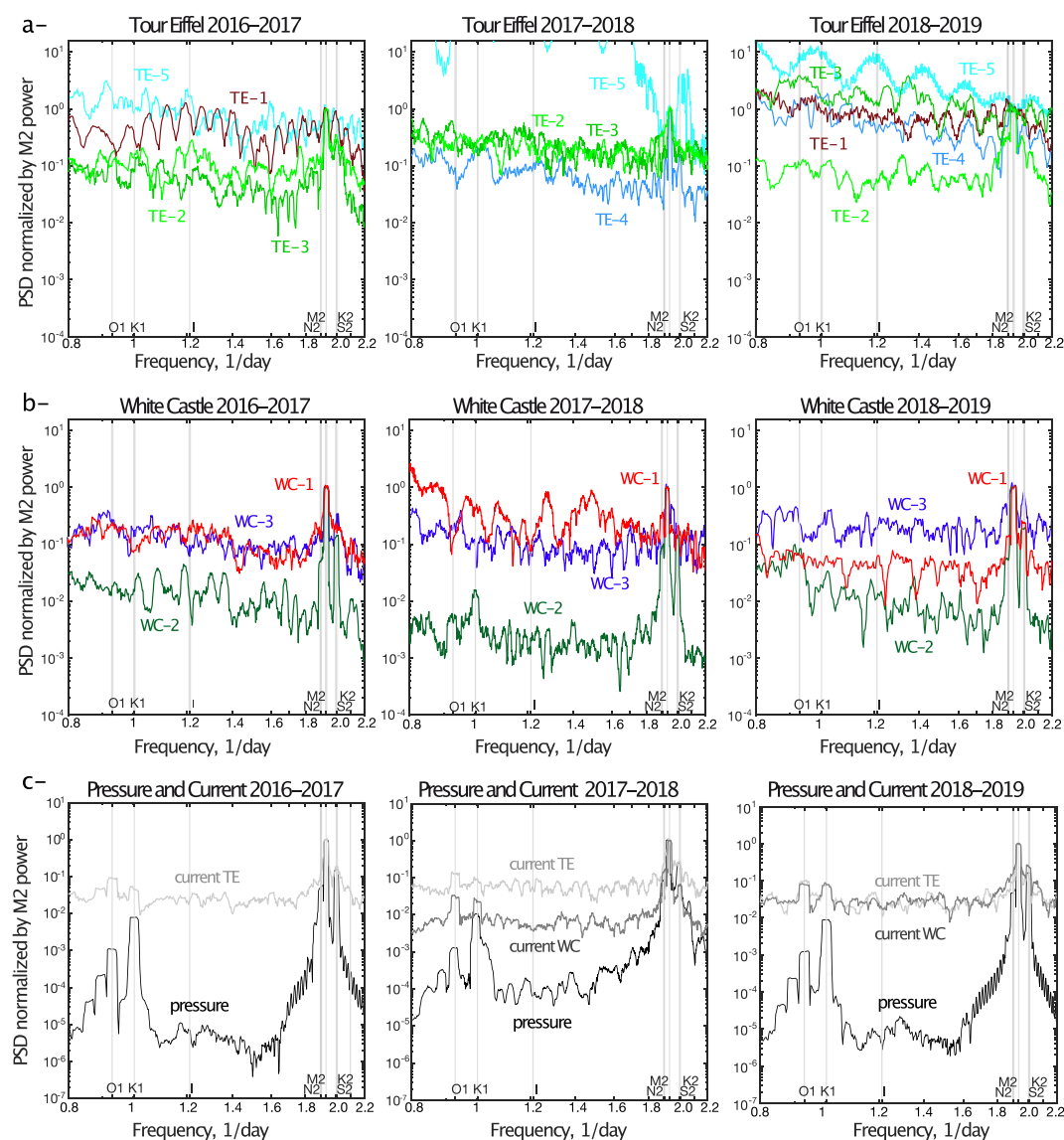
**Figure 8.** (a–c) Power spectrum density (PSD) plots around the diurnal (O1, K1) and semi-diurnal (N2, M2, S2, K2) harmonic peaks for venting temperatures at the TE and WC monitoring locations, for seafloor pressure and for current velocity. PSD values for each time-series are normalized to the PSD value at the M2 semi-diurnal frequency. (a) PSD plots for venting temperatures at TE monitoring locations (red for focused vents, green for diffuse vents in cracks and blue for diffuse vents in sandy areas; PSD values for near seafloor seawater temperatures recorded after the probes fell off the vents are shown in gray). (b) PSD plots for venting temperatures at WC monitoring locations. (c) PSD plots for seafloor pressure and current velocity.

S7b and S7f in Supporting Information S1). In mid to late April 2018, the CM2 maximum at TE-4 coincided with a CM2 maximum for the near bottom seawater temperature recorded by the fallen probe at TE-5 (Figure 7j).

At venting cracks, CM2 values are variable: consistently high (>0.75) at WC-2, except in March 2017 and in September–late October 2018 (Figure 7g), and most commonly low (<0.75) at TE-2 and TE-3 (Figure 7g). The TE-2 and TE-3 cracks are distant by only about 8 m (Figure 5a), yet there is only a weak coincidence between periods of higher CM2 at the two cracks. For example, CM2 are higher at both TE-2 and TE-3 in October 2016, January 2017, May–June 2017, August–September 2017 and late June 2018 (Figure 7g and Figure S7b in Supporting Information S1), but not in early to mid-March 2018 (higher CM2 at TE-3, lower at TE-2) and late March–early April 2018 (lower CM2 at TE-3, higher at TE-2; Figure 7g). During intervals of significant CM2, the amplitude of semi-diurnal temperature variations at venting cracks is variable, both between cracks (semi-diurnal

amplitudes at TE-2 are consistently of several degrees) and at a given crack (a few tens to several degrees at TE-3 and WC-2; Figures 9a and 9b). The largest amplitudes, ~10°C, were recorded at WC-2 in February–March 2018 (Figures 7f and 9b).

PSD values for vent fluid temperatures at the M2 frequency (PSDM2; Figure S5 in Supporting Information S1) carry information on both the coherence and the amplitude of the corresponding semi-diurnal temperature variations. Fortnightly spring tides (Figure S6 in Supporting Information S1) do correspond to some of the PSDM2 maxima: at WC-2, TE-2 and TE-3 in early October 2016; at WC-2, TE-2 and WC3 in mid-March 2017; and in early March 2018 at WC-2 and TE-3 (Figure S5 in Supporting Information S1). However, other PSDM2 maxima correspond to lower amplitude neap tides and PSDM2 values also vary over shorter timescales at the monitored venting cracks and patches, with no correlation, even between nearby vents (Figure S5 in Supporting Information S1).

Phase lags between temperature and pressure at the M2 frequency for periods with CM2 > 0.75 (Figures 7h and 7k and Figures S7c and S7f in Supporting Information S1) are 187–215° at the WC-2 crack in 2016–2017 and 2017–2018, then only 141–164° in 2018–2019, nearly 2 hr less than in the previous 2 years and than at the nearby WC-1 vent over the same time period (Figure 7e and Figure S7h in Supporting Information S1). Phase lags for WC-2 in 2018–2019 also do not show the 1–3 months variations recorded at WC-1 (Figure 7e). Phase lags calculated for venting temperatures during the rare periods of CM2 > 0.75 at the other two monitored cracks (TE-2: 175°–201° in October 2018; and TE-3: 152°–238°; Figure 7h) and at the monitored patches (WC-3: 200°–204° in 2016–2017 and 34°–36° in end-December 2018; and TE-4: 303°–317° in August–early September 2017, then 192°–220° in later periods; Figure 7k), are variable, distinct from one another and distinct from those calculated for the focused fluid at TE-1 (Figure 7e and Figure S7c in Supporting Information S1).

### 6.3. Bottom Current Velocity and Diffuse Venting Temperatures

Current velocities recorded near the TE and WC sites vary between 0.11 and 30 cm.s$^{-1}$ (Figure S8a in Supporting Information S1). Diurnal (O1, K1) and semi-diurnal (N2, M2, S2, K2) tidal related signals carry relatively high energy (Figure 8c). Both the coherence and the PSD at M2 between current velocity and seafloor pressure (Figures S8b and S8d in Supporting Information S1) are variable over timescales of weeks to months and these variations are broadly similar for currentmeters near TE and WC (Figures S8b and S8d in Supporting Information S1). There are, however, significant inter-site differences and also inter-deployments differences in the spectral content of the current velocity records and these probably result in the most part from the location of the currentmeters relative to local relief: contrary to the temperature probes, the TE and WC currentmeters were not set at the same exact same locations from 1 year to the next (Figure 1) and local topography deflects and modifies near bottom currents (Tivey et al., 2002).

Given these local variations, it is likely that if we could deploy currentmeters at individual temperature monitoring locations, their data would also differ, even over distances of meters, because of the rugged topography of the TE and WC sites. Nonetheless, current data available at this point allow us to identify 3 patterns in terms of whether venting temperatures are better correlated with the M2 frequency with seafloor pressure (CM2; Figures 7d, 7g, and 7j) or with local currents (CM2c; Figure S9 in Supporting Information S1). In the first pattern, CM2 is consistently greater than CM2c, suggesting a weaker impact of currents on fluid exit temperature. This is the case at WC-1 in 2018–2019 (Figure 10a) and also at the WC-2 crack for the whole 3 years of monitoring (Figure S10 in Supporting Information S1). In the second pattern, CM2c is significantly greater than CM2, suggesting that tidally modulated variations in current velocity do affect fluid venting temperatures; this is the case at the TE-2 crack for most of the 2018–2019 deployment (Figure 10b). In the third pattern, that is shared by all the other temperature records (Figure S10 in Supporting Information S1), CM2 and CM2c are both low, values >0.75 are uncommon and correspond to either CM2 > CM2c (e.g., at WC-1 in December 2017 and January 2018; Figure 10c) or CM2c > CM2 (e.g., at WC-1 in March 2018 or at TE-2 in October 2017 and February 2018; Figures 10c and 10d).

## 7. Discussion and Conclusions

Our study leads to the following key results and discussion points:
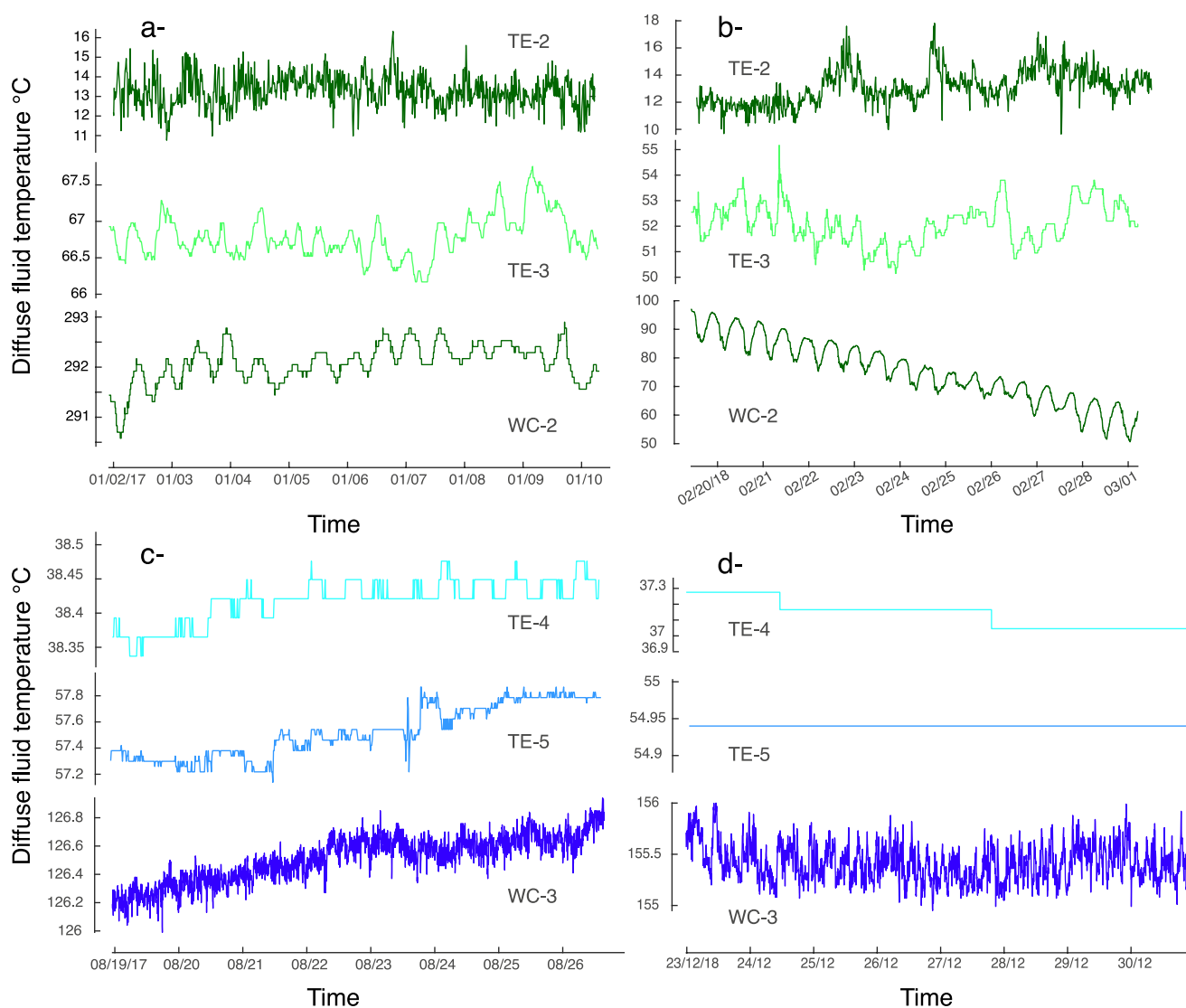
**Figure 9.** Examples of venting temperature variations recorded over a few days at (a and b) venting cracks TE-2, TE-3, and WC-2 and (c and d) venting patches TE-4, TE-5, and WC-3. (a) 2–10 January 2017; (b) 20 February–1 March 2018; (c) 19–26 August 2017; (d) 23–30 December 2018. See the whole temperature records and corresponding values of the coherence between venting temperature and seafloor pressure at the M2 tidal frequency in Figure 7.

1. The chemistry of diffuse fluids collected at the Tour Eiffel and White Castle vent sites points to a complex near seafloor hydrology in which up flowing end-member fluids and entrained seawater are not separated by impermeable barriers. Diffuse fluids contain variable proportions of the black smoker endmember (Figure 6 and Table 1). These fluids are therefore not conductively heated seawater as proposed by Cooper et al. (2000). Also, plotting fluid temperatures against Mg concentrations (used as an indicator of mixing proportions; Figure 6g), suggests in some cases (TE-3 and TE-5 in 2018) simple mixing of seawater with the hot end-member and in other cases some degree of conductive cooling (WC-2 in 2018) or heating (WC-3 in 2016, WC-2 in 2019, TE-3 and TE-5 in 2017 and TE-5 in 2019) of one of the mixed components or of the mixed fluid, prior to venting.

2. The chemistry of diffuse fluids also points to space- and time-variable anhydrite precipitation and dissolution in the substratum of the TE and WC vent sites (Figures 11a and 11b): ongoing anhydrite dissolution in the northern TE substratum is supported by excess dissolved Ca and $SO_4$ at TE-5. WC-3 fluids appear to have undergone anhydrite precipitation in 2016, while the other diffuse fluids analyzed at TE and WC are neither significantly enriched nor depleted in Ca and $SO_4$ (Figures 6e and 6f). Also, many diffuse fluid samples are to some degree depleted in silica, potassium and calcium (Figures 6b–6d). Alteration of basalts to chlorite and
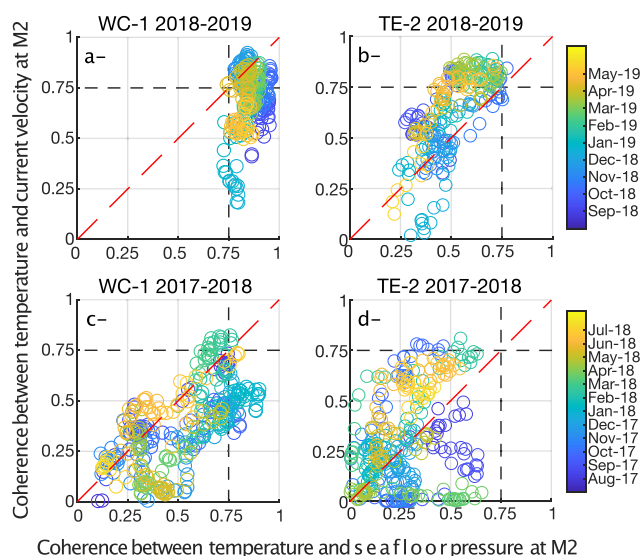
**Figure 10.** Plots showing coherence values at the M2 frequency between venting temperatures and current velocity at monitoring locations WC-1 and TE-2, as a function of their coherence with seafloor pressure also at the M2 frequency. Coherence values are calculated for 30 days sliding window, with a 1 day sliding time. Each dot represents 1 day (dates indicated by color scales). (a) Temperature at focused vent WC-1 in 2018–2019; (b) temperature at diffuse vent in crack TE-2 in 2018–2019; (c) temperature at focused vent WC-1 in 2017–2018; (d) temperature at diffuse vent in crack TE-2 in 2017–2018. Plots for other temperature probes are available in Figure S10 of the Supporting Information S1.

smectite in the upflow domain, as documented at the TAG site (Trans-Atlantic Geotraverse; Sturz et al., 1998), could explain the variable K and Ca depletion, while silica precipitation is documented in the Lucky Strike slab formation (Costa, 2014; Fouquet et al., 1994; Langmuir et al., 1997).

3. A key outcome of our work is to show that the active upflow of end-member rich fluid at both TE and WC corresponds approximately to the domain mapped as slab (Figures 4a and 4b). This represents a significant new constraint on the geometry of site-scale seawater entrainment and mixing (Figures 11a and 11b). Cracks and flanges monitored by the TEMPO ecological module (Sarrazin et al., 2007) on the southern edge of the slab at TE (Figure 5a), vent hot (up to 148°C) and endmember-rich fluids (Laes-Huon et al., 2019). Fluids that vent out of gray patches along the edges of the slab are also rather high temperature and endmember-rich (up to 160°C and E 28% at WC3; Table 1) at both WC (Figure 3e) and TE (Figure 3b). These gray patches had not been identified as venting domains in previous studies of Lucky Strike vent sites. The slab domain is more elongated and smaller (~141 m²) at WC than at TE (~540 m²), but its maximum horizontal extension is not that different between the two sites (25 m at WC against 39 m at TE) and in both cases significantly larger than the sulfide mounds. The narrower elliptical shape of the slab domain at WC (Figure 4b) may result from an intrinsic difference between the two sites, with a more circular upflow domain beneath TE (Figure 4a). Alternatively, the upflow at TE might have a similar NE-trending fault-controlled elliptical shape at depth, with the less-elongated shape of the slab domain there resulting from across strike growth of the shallow stockwork over time. WC sulfide deposits have not been dated, but a contrast in maturity between WC and TE also offers a way to explain the large difference in th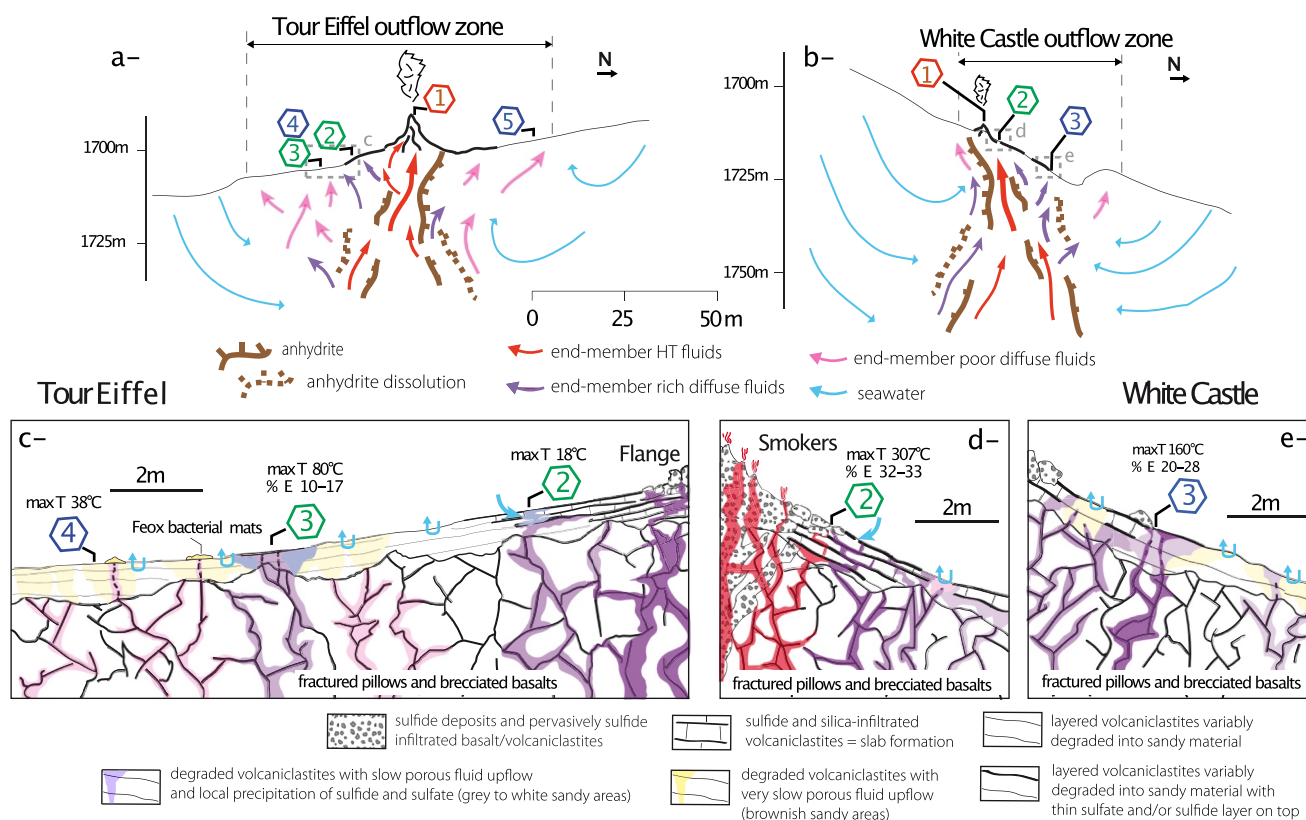e size of the sulfide mounds (8 and 168 m², respectively; Table S2 in Supporting Information S1), the smaller, actively growing WC mound being younger than the larger, 15 m-high TE mound.

4. Our results indicate that diffuse discharge at TE and WC is modified by the <2 m-thick volcaniclastic formation. When cemented by hydrothermal precipitates, this formation acts as an impermeable cap (the slab) over the hydrothermal fluids that come out of the fractured basalt. Venting cracks in the slab probably result from local fracturation and their map distribution is therefore not a good indicator of the upflow patterns in the basalt underneath. In contrast, when not cemented by hydrothermal precipitates, the volcaniclastic formation is porous and the hydrothermal fluids that come out of the fractured basalt ooze through this porous superficial layer, resulting in gray, white and yellowish diffuse venting patches at the seafloor (Figures 11c–11e). The map distribution of these patches (e.g., in Figures 3e and 5a) plausibly results from that of venting cracks in the basalt basement, in which, based on dive observations (e.g., Figure 3e), we propose a decimeter to meter-scale fracture-controlled permeability (Figures 11c and 11e). We further propose that porous advection of the diffuse fluids that come out of the fractured basalts into the smaller scale and more homogeneous permeability of the volcaniclastic layer leads to a widening of the upflow, translating into decreasing diffuse venting velocities and temperatures at the seabed (Figures 11c and 11e). Venting locations TE-3 (gray sandy material in narrow crack; Figure 2c), WC-3 (gray patch; Figure 2h) and TE-5 (yellowish patch; Figure 2e) have shimmering waters indicating significant venting velocities (Mittelstaedt et al., 2012). We propose that they form directly above venting cracks in the underlying basalts (Figures 11c and 11e). Their discharge velocity at the seafloor, their temperature (up to 58°C at TE-5, 80°C at TE-3 and 160°C at WC-3) and their % endmember contribution (up to 17% at TE-3 and TE-5, 28% at WC-3; Table 1) represent lower bounds for the velocity, temperature and composition of the fluids coming out of the basalts underneath.

5. Following on this porous advection interpretation, we propose that the significant spatial and temporal variations in fluid outflow observed in the gray, white and yellowish diffuse venting patches express the porous flow response of the volcaniclastic layer to variations in the temperature and velocity of fluids escaping from meter-spaced cracks in the underlying fractured basalt (Figures 11c and 11d). The distal regions of the porous upflow zones sketched in Figures 11c and 11e correspond to the brownish sandy seabed. Monitoring location

**Figure 11.** Conceptual sketches of near seafloor fluid circulation and diffuse venting at the Tour Eiffel and White Castle sites. (a and b) Are site-scale sketches of hydrothermal circulation patterns at the two vent sites, same scale, no vertical exaggeration, arrows showing possible vent site-scale fluid upflow geometry in the brecciated basalt substratum, with color indicating the relative amount of end-member fluid component, from red (100%), to dark purple, to light purple, to pink and yellow. Fluid upflow zones in red (black-smoker-type fluids) and dark purple (moderately mixed focused flow) have higher temperatures. Fluid upflow zones in light purple to yellow correspond to colder and/or more slowly venting diffuse effluents. Entrained seawater is shown in blue. (c–e) Are detailed geological sketches at monitoring locations TE-2, TE-3, and TE-4 (c), WC-2 (d) and WC-3 (e), located in panels (a) and (b). The maximum recorded temperature and range of estimated % of end-member fluid (% E; Table 1) are shown where available. Colors are indicative of the relative amount of end-member fluid component, as in panels (a) and (b). Layered volcanoclastics and slab cap the brecciated basalt substratum. Permeability pathways in basalts are inferred to be meter-spaced fractures, the slab is impermeable but locally cracked and the non-indurated volcaniclastic formation behaves as a porous medium.

TE-4, in such a brown seabed (Figure 2d), is ~3 m from TE-3 and ~30 cm from a zone of yellowish microbial mats (Figure 5a). There is no visible evidence of fluid venting at TE-4; however, temperatures up to 39° were recorded ~20 cm into the seabed (Figure 7i). If conductive, this temperature gradient would be similar to the highest conductive values measured on the TAG mound (157°C.m$^{-1}$; Becker et al., 1996). However, we favor an interpretation of this strong gradient as due to warm fluids oozing out very slowly through these brownish areas (pale yellow domains in Figures 11c and 11e).

In order to further investigate this, in 2019–2020, we deployed two probes within ~75 cm from each other at the TE-4 location (Figure 12). LTgrad4 in the brown seabed has two iButton temperature sensors (T1 and T2). T2 (~15 cm into the seabed) recorded temperatures of 31.6–36.6°C, with periodic variations over ~140 days, similar to those observed at TE-4 in 2017–2019 (Figure 7i). The other probe (HTNKE38003), ~20 cm into yellow microbial mats (Figure 12a), recorded slightly lower temperatures, also with ~140 days periodic variations, but with a different shape and an offset of ~40–45 days relative to the highs and lows recorded by T2. T1 (~8 cm into the seabed) recorded temperatures of 6–11°C, with a strong semi-diurnal periodicity that was not recovered by the deeper T2 probe (Figure 12d). We interpret this semi-diurnal periodicity as due to tidally modulated entrainment of seawater in the upper decimeter of the seabed and propose that this is a characteristic of brown seabed domains (Figures 11c and 11e), oxydation by entrained seawater possibly explaining their color.

We also propose that temperatures up to 11°C at T1 and 36.6°C at T2 are maintained by the combination of a high conductive heat flux and a very slow upflow of warm fluids, as documented for vents in sediments of the

Yellowstone lake (Sohn & Harris, 2021). We do not have an interpretation at this point for the ∼140 days periodic temperature variations. However, they are probably due to changes in the temperature and/or flux of the fluids that come slowly out of the fractured basalts underneath (Figure 11c). The ∼40–45 days offset between two probes that are only ∼75 cm apart (Figure 12) could then be explained by the lateral propagation of these changes, suggesting lateral fluid velocities of the order of 1 cm/day. A dedicated multiprobe temperature monitoring experiment is underway between locations TE-3 and TE-4 to test these hypotheses.

6. As previously shown by Barreyre et al. (2014a), venting temperatures at Lucky Strike diffuse vents record semi-diurnal variations that are distinct from those at black smokers and are not correlated between vents, even just a few meters apart. These variations mostly display low coherence values with seafloor pressure at the M2 frequency (CM2; Figures 7g and 7j) and variable time lags during high CM2 intervals (Figures 7h and 7k). Their amplitude reaches several degrees at TE-2, TE-3 and WC-2 in 2017–2018 (Figures 9a and 9b) and they are in some cases at least partially controlled by tidally modulated currents (Figure 10b and Barreyre et al., 2014a). Compared to focused vents, diffuse vents therefore display more complex and highly variable tidal forcing effects. We do not attempt to model these effects in terms of possible changes in the porosity structure of the substratum, leaving this more detailed approach for future studies. The added value of our study is to link first-order differences in these tidal responses to the geological setting of the vents and particularly to whether these vents correspond to diffuse patches or cracks.

A common characteristic of the diffuse venting patches monitored in this study (TE-5 and WC-3) and of the brownish surrounding seafloor (TE-4) is that semi-diurnal temperature variations there are weak in both amplitude and coherence at the M2 frequency (Figures 7j and 9c) or absent (within the resolution of the probes; TE-4 and TE-5 yellowish venting patch; Figure 9c). At TE-4, semi-diurnal temperature variations probably result from imperfect damping of tidally modulated seawater entrainment in the upper decimeter of the seabed (as documented by probe T1 in Figure 12). At WC-3 and TE-5, shimmering waters suggest instead that temperature variations are due to changes in the velocity and/or temperature of the upflowing fluids. These variations being weak to absent could mean that the velocity/temperature of fluids coming out of the basalts underneath are not strongly modulated by tides or, and this is our preferred interpretation, that propagation through the porous volcaniclastic layer dampens any tidally modulated temperature signals in the underlying basalt.

Venting cracks (TE-2, TE-3, and WC-2) show more pronounced semi-diurnal temperature variations, with amplitudes up to several degrees (Figures 9a and 9b). Semi-diurnal temperature variations at TE-2 are sometimes better correlated with current velocity than with seafloor pressure (Figure 10b), suggesting that they are caused by currents flushing the crack and the voids that exist between successive layers of slab at this location (Figure 3a) with colder seawater. Venting of high- and lower temperature fluids successively at the same location of the same crack, as seen at WC-2 in 2017–2018 (recorded temperatures between 20 and 217°C; Figure 7f), is also consistent with episodic seawater entrainment in cavities of the slab (Figure 11b). Fluid temperatures are high at WC-2 and tidal variations are strong, even stronger than at the nearby WC-1 black smoker (Figures 7d and 7g), with higher amplitudes (particularly during lower temperature intervals; Figure 9b) and different phase lags (Figures 7e and 7h; Figure S7f in Supporting Information S1). These observations point to a local and shallow process, strongly modulated by seafloor pressure that affects venting temperature and/or velocity in the WC-2 crack. Changes in phase lag such as observed at WC-2 between the 2017–2018 and the 2018–2019 deployments (Figure 7h) may then result from changes in the shallow crack-controlled permeability network in the slab (Figure 11d).

7. Estimates of field- or site scale diffuse heat fluxes at mid-ocean ridge hydrothermal fields carry large uncertainties because diffuse venting areas are complex, with large variations in venting temperature and velocity along a given crack (Mittelstaedt et al., 2012) or patch (this study) and between diffuse vents of the same category (Table S2 in Supporting Information S1). Most of the energy flux in previously published estimates of diffuse heat flux at the Lucky Strike field (195–1,086 MW; Barreyre et al., 2012) or at the Tour Eiffel site (18.75 ± 2.2 MW at TE; Mittelstaedt et al., 2012) comes from the large surface footprint of mounds, patches and flanges, that are grouped in these publications in spite of obvious differences in venting modes (e.g., fluids venting at mounds and flanges are commonly hot enough to cause sulfate-bearing mineral precipitation, but clearly do not vent out of the entire flange surface, while fluids at patches do). However, overestimates of venting surfaces at mounds and flanges in these previous studies are probably somewhat balanced because the authors did not take into account the gray patches documented in this study and used low values of the heat flux
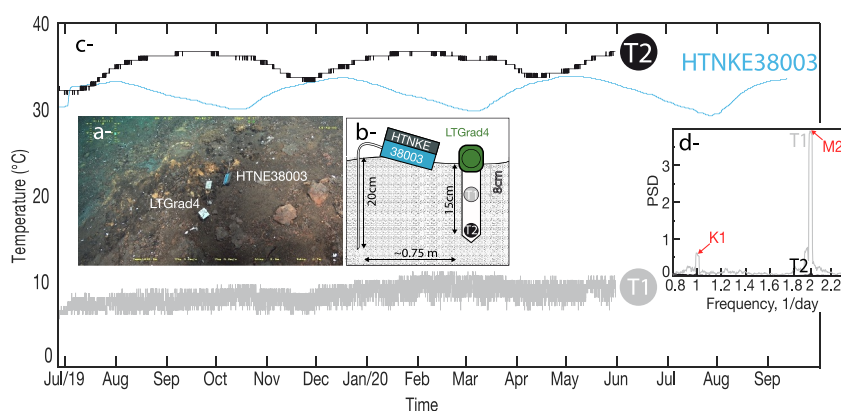
**Figure 12.** Temperature variations recorded with 2 probes experimental setup at and near monitoring location TE-4 in 2019–2020. (a and b) ROV snapshot and sketch showing the experimental setup (HTNKE38003 and LTgrad4 temperature probes). (c) Temperature variations recorded by HTNKE38003 and by the 2 iButton sensors of LTGrad4 (T1 and T2). The shallowest iButton sensor (T1) is about 8 cm into the ground; the deeper one (T2) is about 5 cm shallower than the tip of the HTnke38003 probe. (d) Power spectral density of temperature at diurnal and semi-diurnal frequencies for T1 and T2.

per m$^2$ based on temperatures measured at and not in the seabed (Sarrazin et al., 2009; Table S2 in Supporting Information S1).

We propose a different, yet also rough, approach to estimating these diffuse fluxes. Our study points to relatively hot fluids coming out of the basalt basement at both Tour Eiffel and White Castle, over an area that is about that of the slab domain. Based on the distribution of venting patches in the areas that surround the slab, and on the distribution of fractures in basalt outcrops observed in cliffs near the WC and TE vent sites, we propose that venting fissures and cracks in the basaltic basement are meter-spaced (Figures 11c–11e). We estimate the total surface of such venting cracks as ∼1/100 the total slab surface at both TE and WC (Table S3 in Supporting Information S1). Using an average venting temperature of 140°C (the average temperature at WC-3; Table S2 in Supporting Information S1) and venting velocities of 5–10 mm/s (in the low range of published estimates for Lucky Strike venting cracks; Cooper et al., 2000; Mittelstaedt et al., 2012), we calculate minimum and maximum heat flux values of 14.44 and 28.88 MW and 3.77 and 7.54 MW, respectively, for the diffuse heat flux out of the basaltic basement beneath the slab at TE and WC (Table S4 in Supporting Information S1). To this we add estimated values for off-slab diffuse venting (6.92 and 25.19 MW and 4.48 and 22.41 MW, respectively, for TE and WC), based on the footprint of diffuse patches and on heat flux per m$^2$ values summarized in Table S4 of the Supporting Information S1. All these heat flux values are calculated for temperature dependent fluid density and thermal capacity using the Bischoff and Rosenbauer (1985) seawater equation of state at 200 bar. Total diffuse heat fluxes estimated for Tour Eiffel with this approach (21.36–54.07 MW; 8.25–29.95 MW for White Castle) range between similar to and twice the Mittelstaedt et al. (2012) estimate. Therefore, despite all their respective approximations, the two independent approaches point to diffuse heat fluxes in the same range (several MW, to a few 10s of MW) at the Lucky Strike vent sites, at least 20 times higher than fluxes estimated for focused vents (Barreyre et al., 2012; Mittelstaedt et al., 2012).

## 8. Concluding Remarks

Our results emphasize the complexity of diffuse venting at both Tour Eiffel and White Castle: at least three types of vents, not counting the flanges, with characteristics that are largely controlled by local geology (cracks in the slab, cracks and patches in non-indurated volcaniclastics); variations between nearby vents and in some cases at a given vent, in fluid temperature, degree of mixing and chemical indicators of the precipitation or dissolution of sulfate-bearing minerals; vent temperature variations that are uncorrelated between vents only a few decimeters apart and reveal tidal forcing effects that vary in energy and phase lag, again between nearby vents and also at a given vent through time. Several aspects of the data, including the details of the diffuse fluid chemistry and poroelastic modeling of phase lags at tidal frequencies, are beyond the scope of this paper. While we leave the cause of many of these complexities unresolved, we propose a geologically consistent conceptual framework in

which to interpret this diffuse venting diversity. The thin layer of volcaniclastics that covers the basalts in the Lucky Strike field area plays a key role in this framework, as an intermediate layer, either porous or impermeable depending on whether it has been indurated by hydrothermal precipitates, between the fluids that come out of the basalt basement and the vents at the seafloor. While such a layered volcanic formation is not a standard characteristic of basalt-hosted black smoker hydrothermal systems, our reconstructed picture of the fluids that come out of the fractured basalt basement might be applicable beyond the specific case of Lucky Strike to black smoker sites with similar sizes and fluid fluxes. This reconstructed picture points to venting temperatures >140°C and hydrothermal endmember fluid contribution >20% at distances of at least 15–20 m from the main sulfide mound. We also find that fluids hotter than 80°C and with more than 10% of the hydrothermal endmember component come out of the basalts up to 25 m from the black smokers at both Tour Eiffel and White Castle. This is a significant new constraint on the geometry of site-scale seawater entrainment and mixing in a black smoker system. Based on this better constrained framework, we estimate diffuse heat fluxes that fall in the median to upper range of previously published values for Lucky Strike vent sites.

Our study reports on temperatures measured 8–20 cm into the seabed and the fluids we sampled are not the fluids that surround the seabed fauna: these are further mixed with bottom seawater, that may also carry small amounts of hydrothermal compounds from other vents (Girard et al., 2020; Scheirer et al., 2006; Tivey et al., 2002). Our study thus does not characterize these seabed hydrothermal habitats but brings new constraints on the in-situ hydrothermal effluent component of these complex systems and helps understand their spatial and temporal variations. The next step would be an experimental design that would characterize both this hydrothermal effluent component and the fluids that surround the seabed fauna, at a selection of representative diffuse vents.

## Data Availability Statement

The data on which this article is based are available in Ballu et al. (2021), Cannat et al. (2017), Cannat, Fontaine, et al. (2018), Cannat, Wheeler, et al. (2018), Cannat, Wheeler, Fontaine, et al. (2020), Cannat, Wheeler, Chen, et al. (2020), Cannat et al. (2021a, 2021b), Chavagnac et al. (2023a, 2023b, 2023c, 2023d), Laes-Huon et al. (2019), and Sarradin et al. (2018). Each reference corresponds to a DOI (https://doi.org/10.17882/80573, https://doi.org/10.17882/74195, https://doi.org/10.17882/56428, https://doi.org/10.17882/57005, https://doi.org/10.17882/75412, https://doi.org/10.17882/74378, https://doi.org/10.17882/79527, https://doi.org/10.17882/79528, https://doi.org/10.17882/93198, https://doi.org/10.17882/93197, https://doi.org/10.17882/93196, https://doi.org/10.17882/93192, https://doi.org/10.17882/69883, https://doi.org/10.17882/56522). Each DOI includes metadata and is hosted in SEANOE (SEA scieNtific Open data Edition), an open scientific data repository in the marine science field. SEANOE is operated by the SISMER marine data center within the ODATIS Ocean Cluster framework and funded by Ifremer.

## References

Alt, J. C. (1995). Subseafloor processes in mid-ocean ridge hydrothermal systems. https://doi.org/10.1029/GM091p0085

Andersen, C., Rüpke, L., Hasenclever, J., Grevemeyer, I., & Petersen, S. (2015). Fault geometry and permeability contrast control vent temperatures at the Logatchev 1 hydrothermal field, Mid-Atlantic Ridge. *Geology*, *43*(1), 51–54. https://doi.org/10.1130/g36113.1

Arnulf, A. F., Harding, A. J., Singh, S. C., Kent, G. M., & Crawford, W. C. (2014). Nature of upper crust beneath the Lucky Strike volcano using elastic full waveform inversion of streamer data. *Geophysical Journal International*, *196*(3), 1471–1491. https://doi.org/10.1093/gji/ggt461

Astorch-Cardona, A., Guerre, M., Dola, A., Chavagnac, V., & Rommevaux, C. (2023). Spatial comparison and temporal evolution of two iron-rich microbial mats from the Lucky Strike hydrothermal field, related to environmental variations. *Frontiers in Marine Science*. https://doi.org/10.3389/fmars.2023.1038192

Baker, E. T., Massoth, G. J., Walker, S. L., & Embley, R. W. (1993). A method for quantitatively estimating diffuse and discrete hydrothermal discharge. *Earth and Planetary Science Letters*, *118*(1–4), 235–249. https://doi.org/10.1016/0012-821x(93)90170-e

Ballu, V., Cannat, M., Wheeler, B., Legrand, J., & Sarradin, P.-M. (2021). Seafloor pressure data from two SBE53 pressure gauges on EMSO-Azores observatory, 2019-2020 [Dataset]. SEANOE. https://doi.org/10.17882/80573

Barreyre, T., Escartín, J., Garcia, R., Cannat, M., Mittelstaedt, E., & Prados, R. (2012). Structure, temporal evolution and heat flux estimates from the Lucky Strike deep-sea hydrothermal field derived from seafloor image mosaics. *Geochemistry, Geophysics, Geosystems*, *13*(4), Q04007. https://doi.org/10.1029/2011gc003990

Barreyre, T., Escartín, J., Sohn, R., & Cannat, M. (2014b). Permeability of the Lucky Strike deep-sea hydrothermal system: Constraints from the poroelastic response to ocean tidal loading. *Earth and Planetary Science Letters*, *408*, 146–154. https://doi.org/10.1016/j.epsl.2014.09.049

Barreyre, T., Escartín, J., Sohn, R. A., Cannat, M., Ballu, V., & Crawford, W. C. (2014a). Temporal variability and tidal modulation of hydrothermal exit-fluid temperatures at the Lucky Strike deep-sea vent field, Mid-Atlantic Ridge. *Journal of Geophysical Research: Solid Earth*, *119*(4), 2543–2566. https://doi.org/10.1002/2013jb010478

Barreyre, T., Olive, J., Crone, T. J., & Sohn, R. A. (2018). Depth-dependent permeability and heat output at basalt-hosted hydrothermal systems across mid-ocean ridge spreading rates. *Geochemistry, Geophysics, Geosystems*, *19*(4), 1259–1281. https://doi.org/10.1002/2017gc007152

Barreyre, T., Parnell-Turner, R., Wu, J.-N., & Fornari, D. J. (2022). Tracking crustal permeability and hydrothermal response during seafloor eruptions at the East Pacific Rise, 9°50′N. *Geophysical Research Letters*, *49*(3), e2021GL095459. https://doi.org/10.1029/2021gl095459

Barreyre, T., & Sohn, R. A. (2016). Poroelastic response of mid-ocean ridge hydrothermal systems to ocean tidal loading: Implications for shallow permeability structure. *Geophysical Research Letters*, *43*(4), 1660–1668. https://doi.org/10.1002/2015gl066479

Becker, K., Herzen, R. V., Kirklin, J., Evans, R., Kadko, D., Kinoshita, M., et al. (1996). Conductive heat flow at the TAG active hydrothermal mound: Results from 1993–1995 submersible surveys. *Geophysical Research Letters*, *23*(23), 3463–3466. https://doi.org/10.1029/96gl00969

Bemis, K., Lowell, R., & Farough, A. (2012). Diffuse flow on and around hydrothermal vents at mid-ocean ridges. *Oceanography*, *25*(1), 182–191. https://doi.org/10.5670/oceanog.2012.16

Besson, P., Degboe, J., Berge, B., Chavagnac, V., Fabre, S., & Berger, G. (2014). Calcium, Na, K and Mg concentrations in seawater by inductively coupled plasma-atomic emission spectrometry: Applications to IAPSO seawater reference material, hydrothermal fluids and synthetic seawater solutions. *Geostandards and Geoanalytical Research*, *38*(3), 355–362. https://doi.org/10.1111/j.1751-908x.2013.00269.x

Bischoff, J. L., & Rosenbauer, R. J. (1985). An empirical equation of state for hydrothermal seawater (3.2 percent NaCl). *American Journal of Science*, *285*(8), 725–763. https://doi.org/10.2475/ajs.285.8.725

Bischoff, J. L., & Seyfried, W. E. (1978). Hydrothermal chemistry of seawater from 25 degrees to 350 degrees C. *American Journal of Science*, *278*(6), 838–860. https://doi.org/10.2475/ajs.278.6.838

Butterfield, D. A., Roe, K. K., Lilley, M. D., Huber, J. A., Baross, J. A., Embley, R. W., & Massoth, G. J. (2004). Mixing, reaction and microbial activity in the sub-seafloor revealed by temporal and spatial variation in diffuse flow vents at axial volcano. *Geophysical Monograph Series*, 269–289. https://doi.org/10.1029/144gm17

Cann, J. R., & Strens, M. R. (1982). Black smokers fuelled by freezing magma. *Nature*, *298*(5870), 147–149. https://doi.org/10.1038/298147a0

Cannat, M., Fontaine, F. J., Barreyre, T., Wheeler, B., Escartin, J., & Sarradin, P.-M. (2018). Autonomous temperature probes, data from the EMSO-Azores observatory, 2016-2017 [Dataset]. SEANOE. https://doi.org/10.17882/56428

Cannat, M., Wheeler, B., Barreyre, T., & Sarradin, P.-M. (2017). Array of ocean bottom tilt current meters: Data from the EMSO-Azores observatory, 2016-2017 [Dataset]. SEANOE. https://doi.org/10.17882/74195

Cannat, M., Wheeler, B., Chen, J., Sarradin, P.-M., & Legrand, J. (2020). Array of ocean bottom tilt current meters: Data from the EMSO-Azores observatory, 2018-2019 [Dataset]. SEANOE. https://doi.org/10.17882/74378

Cannat, M., Wheeler, B., Fontaine, F., Chen, J., & Sarradin, P.-M. (2021b). Autonomous temperature probes, data from the EMSO-Azores observatory, 2019-2020 [Dataset]. SEANOE. https://doi.org/10.17882/79528

Cannat, M., Wheeler, B., Fontaine, F., Chen, J., Sarradin, P.-M., & Legrand, J. (2021a). Autonomous temperature probes, data from the EMSO-Azores observatory, 2018-2019 [Dataset]. SEANOE. https://doi.org/10.17882/79527

Cannat, M., Wheeler, B., Fontaine, F. J., Rouméjon, S., Sarradin, P.-M., & Legrand, J. (2020). Autonomous temperature probes, data from the EMSO-Azores observatory, 2017-2018 [Dataset]. SEANOE. https://doi.org/10.17882/75412

Cannat, M., Wheeler, B., Rouméjon, S., Sarradin, P.-M., & Legrand, J. (2018). Array of ocean bottom tilt current meters: Data from the EMSO-Azores observatory, 2017-2018 [Dataset]. SEANOE. https://doi.org/10.17882/57005

Charlou, J. L., Donval, J. P., Douville, E., Jean-Baptiste, P., Radford-Knoery, J., Fouquet, Y., et al. (2000). Compared geochemical signatures and the evolution of Menez Gwen (37°50′N) and Lucky Strike (37°17′N) hydrothermal fluids, south of the Azores Triple Junction on the Mid-Atlantic Ridge. *Chemical Geology*, *171*(1–2), 49–75. https://doi.org/10.1016/s0009-2541(00)00244-8

Chavagnac, V., Christine, D., & Castillo, A. (2023a). Geochemistry of hydrothermal fluids at the Lucky Strike hydrothermal field data from the EMSO-Azores observatory, 2016 [Dataset]. SEANOE. https://doi.org/10.17882/93198

Chavagnac, V., Christine, D., & Castillo, A. (2023b). Geochemistry of hydrothermal fluids at the Lucky Strike hydrothermal field data from the EMSO-Azores observatory, 2017 [Dataset]. SEANOE. https://doi.org/10.17882/93197

Chavagnac, V., Christine, D., & Castillo, A. (2023c). Geochemistry of hydrothermal fluids at the Lucky Strike hydrothermal field data from the EMSO-Azores observatory, 2018 [Dataset]. SEANOE. https://doi.org/10.17882/93196

Chavagnac, V., Christine, D., & Castillo, A. (2023d). Geochemistry of hydrothermal fluids at the Lucky Strike hydrothermal field data from the EMSO-Azores observatory, 2019 [Dataset]. SEANOE. https://doi.org/10.17882/93192

Chavagnac, V., Leleu, T., Fontaine, F., Cannat, M., Ceuleneer, G., & Castillo, A. (2018). Spatial variations in vent chemistry at the lucky strike hydrothermal field, Mid-Atlantic Ridge (37°N): Updates for subseafloor flow geometry from the newly discovered Capelinhos Vent. *Geochemistry, Geophysics, Geosystems*, *19*(11), 4444–4458. https://doi.org/10.1029/2018gc007765

Colaço, A., Blandin, J., Cannat, M., Carval, T., Chavagnac, V., Connelly, D., et al. (2011). MoMAR-D: A technological challenge to monitor the dynamics of the Lucky Strike vent ecosystem. *ICES Journal of Marine Science*, *68*(2), 416–424. https://doi.org/10.1093/icesjms/fsq075

Combier, V., Seher, T., Singh, S. C., Crawford, W. C., Cannat, M., Escartín, J., & Dusunur, D. (2015). Three-dimensional geometry of axial magma chamber roof and faults at Lucky Strike volcano on the Mid-Atlantic Ridge. *Journal of Geophysical Research: Solid Earth*, *120*(8), 5379–5400. https://doi.org/10.1002/2015jb012365

Converse, D. R., Holland, H. D., & Edmond, J. M. (1984). Flow rates in the axial hot springs of the East Pacific Rise (21°N): Implications for the heat budget and the formation of massive sulfide deposits. *Earth and Planetary Science Letters*, *69*(1), 159–175. https://doi.org/10.1016/0012-821x(84)90080-3

Cooper, M. J., Elderfield, H., & Schultz, A. (2000). Diffuse hydrothermal fluids from Lucky Strike hydrothermal vent field: Evidence for a shallow conductively heated system. *Journal of Geophysical Research*, *105*(B8), 19369–19375. https://doi.org/10.1029/2000jb900138

Corliss, J. B., Dymond, J., Gordon, L. I., Edmond, J. M., von Herzen, R. P., Ballard, R. D., et al. (1979). Submarine thermal sprirngs on the Galápagos Rift. *Science*, *203*(4385), 1073–1083. https://doi.org/10.1126/science.203.4385.1073

Costa, I. (2014). Genesis of the brecciated rocks from Mid Atlantic Ridge hydrothermal systems: Lucky Strike (37°50′N) and Menez Gwen (37°50′N). Ph.D. thesis. Lisbon University, Science Faculty, Geology department. Retrieved from http://hdl.handle.net/10451/11413

Coumou, D., Driesner, T., & Heinrich, C. A. (2008). The structure and dynamics of mid-ocean ridgeydrothermal systems. *Science*, *321*(5897), 1825–1828. https://doi.org/10.1126/science.1159582

Crawford, W. C., Rai, A., Singh, S. C., Cannat, M., Escartin, J., Wang, H., et al. (2013). Hydrothermal seismicity beneath the summit of Lucky Strike volcano, Mid-Atlantic Ridge. *Earth and Planetary Science Letters*, *373*, 118–128. https://doi.org/10.1016/j.epsl.2013.04.028

Crawford, W. C., Singh, S. C., Seher, T., Combier, V., Dogan, D. D., & Cannat, M. (2010). Crustal structure, magma chamber and faulting beneath the Lucky Strike hydrothermal vent field. In *American geophysical union geophysical monograph series*. https://doi.org/10.1029/2008gm000726

Crépeau, V., Bonavita, M. C., Lesongeur, F., Randrianalivelo, H., Sarradin, P., Sarrazin, J., & Godfroy, A. (2011). Diversity and function in microbial mats from the Lucky Strike hydrothermal vent field. *FEMS Microbiology Ecology*, *76*(3), 524–540. https://doi.org/10.1111/j.1574-6941.2011.01070.x

Crone, T. J., & Wilcock, W. S. D. (2005). Modeling the effects of tidal loading on mid-ocean ridge hydrothermal systems. *Geochemistry, Geophysics, Geosystems*, *6*(7), Q07001. https://doi.org/10.1029/2004gc000905

Cuvelier, D., Sarrazin, J., Colaço, A., Copley, J., Desbruyères, D., Glover, A. G., et al. (2009). Distribution and spatial variation of hydrothermal faunal assemblages at Lucky Strike (Mid-Atlantic Ridge) revealed by high-resolution video image analysis. *Deep Sea Research Part I: Oceanographic Research Papers*, *56*(11), 2026–2040. https://doi.org/10.1016/j.dsr.2009.06.006

Dover, C. L. V., Desbruyères, D., Segonzac, M., Comtet, T., Saldanha, L., Fiala-Medioni, A., & Langmuir, C. (1996). Biology of the Lucky Strike hydrothermal field. *Deep Sea Research Part I: Oceanographic Research Papers*, *43*(9), 1509–1529. https://doi.org/10.1016/s0967-0637(96)00051-9

Edmond, J. M., Campbell, A. C., Palmer, M. R., Klinkhammer, G. P., German, C. R., Edmonds, H. N., et al. (1995). Time series studies of vent fluids from the TAG and MARK sites (1986, 1990) Mid-Atlantic Ridge: A new solution chemistry model and a mechanism for Cu/Zn zonation in massive sulphide orebodies. *Geological Society, London, Special Publications*, *87*(1), 77–86. https://doi.org/10.1144/gsl.sp.1995.087.01.07

Edmond, J. M., Measures, C., McDuff, R. E., Chan, L. H., Collier, R., Grant, B., et al. (1979). Ridge crest hydrothermal activity and the balances of the major and minor elements in the ocean: The Galapagos data. *Earth and Planetary Science Letters*, *46*(1), 1–18. https://doi.org/10.1016/0012-821x(79)90061-x

Eissen, J. P., Fouquet, Y., Hardy, D., & Ondréas, H. (2003). Recent MORB volcaniclastic explosive deposits formed between 500 and 1750 m.b.s. l. on the axis of the Mid-Atlantic Ridge, south of the Azores. In J. D. L. White, J. L. Smellie, & D. A. Clague (Eds.), *Explosive subaqueous volcanism, geophysical monograph series* (Vol. 140, pp. 143–166). AGU. https://doi.org/10.1029/140GM09

Elderfield, H., & Schultz, A. (1996). Mid-ocean ridge hydrothermal fluxes and the chemical composition of the ocean. *Earth and Planetary Sciences*, *24*(1), 191–224. https://doi.org/10.1146/annurev.earth.24.1.191

Embley, R. W., Murphy, K. M., & Fox, C. G. (1990). High-resolution studies of the summit of Axial Volcano. *Journal of Geophysical Research*, *95*(B8), 12785–12812. https://doi.org/10.1029/jb095ib08p12785

Escartin, J., Barreyre, T., Cannat, M., Garcia, R., Gracias, N., Deschamps, A., et al. (2015). Hydrothermal activity along the slow-spreading Lucky Strike ridge segment (Mid-Atlantic Ridge): Distribution, heatflux and geological controls. *Earth and Planetary Science Letters*, *431*, 173–185. https://doi.org/10.1016/j.epsl.2015.09.025

Escartín, J., Soule, S. A., Cannat, M., Fornari, D. J., Düşünür, D., & Garcia, R. (2014). Lucky Strike seamount: Implications for the emplacement and rifting of segment-centered volcanoes at slow spreading mid-ocean ridges. *Geochemistry, Geophysics, Geosystems*, *15*(11), 4157–4179. https://doi.org/10.1002/2014gc005477

Field, M. P., & Sherrell, R. M. (2000). Dissolved and particulate Fe in a hydrothermal plume at 9°45′N, East Pacific Rise: Slow Fe (II) oxidation kinetics in Pacific plumes. *Geochimica et Cosmochimica Acta*, *64*(4), 619–628. https://doi.org/10.1016/s0016-7037(99)00333-6

Fontaine, F. J., Cannat, M., Escartin, J., & Crawford, W. C. (2014). Along-axis hydrothermal flow at the axis of slow spreading mid-ocean ridges: Insights from numerical models of the Lucky Strike vent field (MAR). *Geochemistry, Geophysics, Geosystems*, *15*(7), 2918–2931. https://doi.org/10.1002/2014gc005372

Fouquet, Y., Charlou, J.-L., Costa, I., Donval, J.-P., Radford-Knoery, J., Pellé, H., et al. (1994). *A detailed study of the Lucky Strike hydrothermal site and discovery of a new hydrothermal site: Menez Gwen; preliminary results of the DIVA1 cruise (5-29 May, 1994)*. InterRidge News.

Foustoukos, D. I., Pester, N. J., Ding, K., & Seyfried, W. E. (2009). Dissolved carbon species in associated diffuse and focused flow hydrothermal vents at the Main Endeavour Field, Juan de Fuca Ridge: Phase equilibria and kinetic constraints. *Geochemistry, Geophysics, Geosystems*, *10*(10), Q10003. https://doi.org/10.1029/2009gc002472

Gamo, T., Chiba, H., Masuda, H., Edmonds, H. N., Fujioka, K., Kodama, Y., et al. (1996). Chemical characteristics of hydrothermal fluids from the TAG Mound of the Mid-Atlantic Ridge in August 1994: Implications for spatial and temporal variability of hydrothermal activity. *Geophysical Research Letters*, *23*(23), 3483–3486. https://doi.org/10.1029/96gl02521

Ginster, U., Mottl, M. J., & Herzen, R. P. V. (1994). Heat flux from black smokers on the Endeavour and Cleft segments, Juan de Fuca Ridge. *Journal of Geophysical Research*, *99*(B3), 4937–4950. https://doi.org/10.1029/93jb02800

Girard, F., Sarrazin, J., Arnaubec, A., Cannat, M., Sarradin, P.-M., Wheeler, B., & Matabos, M. (2020). Currents and topography drive assemblage distribution on an active hydrothermal edifice. *Progress in Oceanography*, *187*, 102397. https://doi.org/10.1016/j.pocean.2020.102397

Glickson, D. A., Kelley, D. S., & Delaney, J. R. (2007). Geology and hydrothermal evolution of the Mothra hydrothermal field, Endeavour segment, Juan de Fuca Ridge. *Geochemistry, Geophysics, Geosystems*, *8*(6), Q06010. https://doi.org/10.1029/2007gc001588

Guo, Z., Rüpke, L. H., Fuchs, S., Iyer, K., Hannington, M. D., Chen, C., et al. (2020). Anhydrite-assisted hydrothermal metal transport to the ocean floor—Insights from thermo-hydro-chemical modeling. *Journal of Geophysical Research: Solid Earth*, *125*(7), e2019JB019035. https://doi.org/10.1029/2019jb019035

Hawkes, J. A., Connelly, D. P., Gledhill, M., & Achterberg, E. P. (2013). The stabilisation and transportation of dissolved iron from high temperature hydrothermal vent systems. *Earth and Planetary Science Letters*, *375*, 280–290. https://doi.org/10.1016/j.epsl.2013.05.047

Holden, J. F., & Daniel, R. M. (2004). The upper temperature limit for life based on hyperthermophile culture experiments and field observations, 13–24. https://doi.org/10.1029/144gm02

Humphris, S. E., Fornari, D. J., Scheirer, D. S., German, C. R., & Parson, L. M. (2002). Geotectonic setting of hydrothermal activity on the summit of Lucky Strike Seamount (37°17′N, Mid-Atlantic Ridge). *Geochemistry, Geophysics, Geosystems*, *3*(8), 1–25. https://doi.org/10.1029/2001gc000284

Humphris, S. E., Herzig, P. M., Miller, D. J., Alt, J. C., Becker, K., Brown, D., et al. (1995). The internal structure of an active sea-floor massive sulphide deposit. *Nature*, *377*(6551), 713–716. https://doi.org/10.1038/377713a0

James, R. H., & Elderfield, H. (1996). Chemistry of ore-forming fluids and mineral formation rates in an active hydrothermal sulfide deposit on the Mid-Atlantic Ridge. *Geology*, *24*(12), 1147–1150. https://doi.org/10.1130/0091-7613(1996)024<1147:cooffa>2.3.co;2

Jannasch, H. W., & Mottl, M. J. (1985). Geomicrobiology of deep-sea hydrothermal vents. *Science*, *229*(4715), 717–725. https://doi.org/10.1126/science.229.4715.717

Juniper, S. K., Martineu, P., Sarrazin, J., & Gélinas, Y. (1995). Microbial-mineral floc associated with nascent hydrothermal activity on CoAxial Segment, Juan de Fuca Ridge. *Geophysical Research Letters*, *22*(2), 179–182. https://doi.org/10.1029/94gl02436

Jupp, T. E., & Schultz, A. (2004). A poroelastic model for the tidal modulation of seafloor hydrothermal systems. *Journal of Geophysical Research*, *109*(B3), B03105. https://doi.org/10.1029/2003jb002583

Kelley, D. S., Baross, J. A., & Delaney, J. R. (2002). Volcanoes, fluids and life at mid-ocean ridge spreading centers. *Annual Review of Earth and Planetary Sciences*, *30*(1), 385–491. https://doi.org/10.1146/annurev.earth.30.091201.141331

Koschinsky, A., Seifert, R., Halbach, P., Bau, M., Brasse, S., de Carvalho, L. M., & Fonseca, N. M. (2002). Geochemistry of diffuse low-temperature hydrothermal fluids in the North Fiji basin. *Geochimica et Cosmochimica Acta*, *66*(8), 1409–1427. https://doi.org/10.1016/s0016-7037(01)00855-9

Laes-Huon, A., Sarradin, P.-M., & Cannat, M. (2019). CHEMINI total dissolved iron concentrations from the EMSO-Azores observatory, 2018-2019 [Dataset]. SEANOE. https://doi.org/10.17882/69883

Langmuir, C., Fornari, D., Colodner, D., Charlou, J., Costa, I., Desbruyeres, D., et al. (1993). Geological setting and characteristics of the Lucky Strike vent field at 37°17′N on the Mid-Atlantic Ridge. *Eos, Transactions American Geophysical Union*, *74*(43), 99.

Langmuir, C., Humphris, S., Fornari, D., Dover, C. V., Damm, K. V., Tivey, M. K., et al. (1997). Hydrothermal vents near a mantle hot spot: The Lucky Strike vent field at 37°N on the Mid-Atlantic Ridge. *Earth and Planetary Science Letters*, *148*(1–2), 69–91. https://doi.org/10.1016/s0012-821x(97)00027-7

Larson, B., Olson, E., & Lilley, M. (2007). In situ measurement of dissolved chloride in high temperature hydrothermal fluids. *Geochimica et Cosmochimica Acta*, *71*(10), 2510–2523. https://doi.org/10.1016/j.gca.2007.02.013

Larson, B. I., Houghton, J. L., Lowell, R. P., Farough, A., & Meile, C. D. (2015). Subsurface conditions in hydrothermal vents inferred from diffuse flow composition and models of reaction and transport. *Earth and Planetary Science Letters*, *424*, 245–255. https://doi.org/10.1016/j.epsl.2015.05.033

Lister, C. R. B. (1972). On the thermal balance of a mid-ocean ridge. *Geophysical Journal of the Royal Astronomical Society*, *26*(5), 515–535. https://doi.org/10.1111/j.1365-246x.1972.tb05766.x

Lister, C. R. B. (1974). On the penetration of water into hot rock. *Geophysical Journal International*, *39*(3), 465–509. https://doi.org/10.1111/j.1365-246x.1974.tb05468.x

Little, S. A., Stolzenbach, K. D., & Grassle, F. J. (1988). Tidal current effects on temperature in diffuse hydrothermal flow: Guaymas Basin. *Geophysical Research Letters*, *15*(13), 1491–1494. https://doi.org/10.1029/gl015i013p01491

Lowell, R. P., Rona, P. A., & Herzen, R. P. V. (1995). Seafloor hydrothermal systems. *Journal of Geophysical Research*, *100*(B1), 327–352. https://doi.org/10.1029/94jb02222

Lowell, R. P., Farough, A., Germanovich, L., Hebert, L., & Horne, R. (2012). A vent-field-scale model of the East Pacific Rise 9°50′N magma-hydrothermal system. *Oceanography*, *25*(1), 158–167. https://doi.org/10.5670/oceanog.2012.13

Lowell, R. P., Gosnell, S., & Yang, Y. (2007). Numerical simulations of single-pass hydrothermal convection at mid-ocean ridges: Effects of the extrusive layer and temperature-dependent permeability. *Geochemistry, Geophysics, Geosystems*, *8*(10), Q10011. https://doi.org/10.1029/2007gc001653

Lowell, R. P., Houghton, J. L., Farough, A., Craft, K. L., Larson, B. I., & Meile, C. D. (2015). Mathematical modeling of diffuse flow in seafloor hydrothermal systems: The potential extent of the subsurface biosphere at mid-ocean ridges. *Earth and Planetary Science Letters*, *425*, 145–153. https://doi.org/10.1016/j.epsl.2015.05.047

Lowell, R. P., & Yao, Y. (2002). Anhydrite precipitation and the extent of hydrothermal recharge zones at ocean ridge crests. *Journal of Geophysical Research*, *107*(B9), EPM2-1–EPM2-9. https://doi.org/10.1029/2001jb001289

Lowell, R. P., Yao, Y., & Germanovich, L. N. (2003). Anhydrite precipitation and the relationship between focused and diffuse flow in seafloor hydrothermal systems. *Journal of Geophysical Research*, *108*(B9), 2424. https://doi.org/10.1029/2002jb002371

Matabos, M., Barreyre, T., Juniper, S. K., Cannat, M., Kelley, D., Alfaro-Lucas, J. M., et al. (2022). Integrating multidisciplinary observations in vent environments (IMOVE): Decadal progress in deep-sea observatories at hydrothermal vents. *Frontiers in Marine Science*, *9*, 866422. https://doi.org/10.3389/fmars.2022.866422

Millero, F. J., Feistel, R., Wright, D. G., & McDougall, T. J. (2008). The composition of standard seawater and the definition of the reference-composition salinity scale. *Deep Sea Research Part I: Oceanographic Research Papers*, *55*(1), 50–72. https://doi.org/10.1016/j.dsr.2007.10.001

Miranda, J. M., Luis, J. F., Lourenço, N., & Santos, F. M. (2005). Identification of the magnetization low of the Lucky Strike hydrothermal vent using surface magnetic data. *Journal of Geophysical Research*, *110*(B4), B04103. https://doi.org/10.1029/2004jb003085

Mittelstaedt, E., Escartín, J., Gracias, N., Olive, J., Barreyre, T., Davaille, A., et al. (2012). Quantifying diffuse and discrete venting at the Tour Eiffel vent site, Lucky Strike hydrothermal field. *Geochemistry, Geophysics, Geosystems*, *13*(4), Q04008. https://doi.org/10.1029/2011gc003991

Mittelstaedt, E., Fornari, D. J., Crone, T. J., Kinsey, J., Kelley, D., & Elend, M. (2016). Diffuse venting at the ASHES hydrothermal field: Heat flux and tidally modulated flow variability derived from in situ time-series measurements. *Geochemistry, Geophysics, Geosystems*, *17*(4), 1435–1453. https://doi.org/10.1002/2015gc006144

Ondréas, H., Cannat, M., Fouquet, Y., Normand, A., Sarradin, P. M., & Sarrazin, J. (2009). Recent volcanic events and the distribution of hydrothermal venting at the Lucky Strike hydrothermal field, Mid-Atlantic Ridge. *Geochemistry, Geophysics, Geosystems*, *10*(2), Q02006. https://doi.org/10.1029/2008gc002171

Percival, D. B., & Walden, A. T. (1993). *Spectral analysis for physical applications*. Cambridge University Press. https://doi.org/10.1017/cbo9780511622762

Pester, N. J., Reeves, E. P., Rough, M. E., Ding, K., Seewald, J. S., & Seyfried, W. E. (2012). Subseafloor phase equilibria in high-temperature hydrothermal fluids of the Lucky Strike Seamount (Mid-Atlantic Ridge, 37°17′N). *Geochimica et Cosmochimica Acta*, *90*, 303–322. https://doi.org/10.1016/j.gca.2012.05.018

Pruis, M. J., & Johnson, H. P. (2004). Tapping into the sub-seafloor: Examining diffuse flow and temperature from an active seamount on the Juan de Fuca Ridge. *Earth and Planetary Science Letters*, *217*(3–4), 379–388. https://doi.org/10.1016/s0012-821x(03)00607-1

Ramondenc, P., Germanovich, L. N., Damm, K. L. V., & Lowell, R. P. (2006). The first measurements of hydrothermal heat output at 9°50′N, East Pacific Rise. *Earth and Planetary Science Letters*, *245*(3–4), 487–497. https://doi.org/10.1016/j.epsl.2006.03.023

Rona, P. A., & Trivett, D. A. (1992). Discrete and diffuse heat transfer atashes vent field, Axial Volcano, Juan de Fuca Ridge. *Earth and Planetary Science Letters*, *109*(1–2), 57–71. https://doi.org/10.1016/0012-821x(92)90074-6

Rouxel, O., Fouquet, Y., & Ludden, J. N. (2004a). Copper isotope systematics of the Lucky Strike, rainbow and Logatchev sea-floor hydrothermal fields on the Mid-Atlantic Ridge. *Economic Geology*, *99*(3), 585–600. https://doi.org/10.2113/gsecongeo.99.3.585

Rouxel, O., Fouquet, Y., & Ludden, J. N. (2004b). Subsurface processes at the lucky strike hydrothermal field, Mid-Atlantic Ridge: Evidence from sulfur, selenium and iron isotopes. *Geochimica et Cosmochimica Acta*, *68*(10), 2295–2311. https://doi.org/10.1016/j.gca.2003.11.029

Sánchez-Mora, D., Jamieson, J., Cannat, M., Escartín, J., & Barreyre, T. (2022). Effects of substrate composition and subsurface fluid pathways on the geochemistry of seafloor hydrothermal deposits at the Lucky Strike Vent Field, Mid-Atlantic Ridge. *Geochemistry, Geophysics, Geosystems*, *23*(5), e2021GC010073. https://doi.org/10.1029/2021gc010073

Sarradin, P.-M., Caprais, J.-C., Riso, R., Kerouel, R., & Aminot, A. (1999). Chemical environment of the hydrothermal mussel communities in the Lucky Strike and Menez Gwen vent fields, Mid Atlantic Ridge. Retrieved from https://archimer.ifremer.fr/doc/00147/25847/

Sarradin, P.-M., Legrand, J., Moreau, B., Lanteri, N., & Cannat, M. (2018). High precision pressure, data from the EGIM deployed on EMSO-Azores observatory, 2017-2018 [Dataset]. SEANOE. https://doi.org/10.17882/56522

Sarrazin, J., Blandin, J., Delauney, L., Dentrecolas, S., Dorval, P., Dupont, J., et al. (2007). TEMPO: A new ecological module for studying deep-sea community dynamics at hydrothermal vents. *OCEANS 2007—Europe*, 1–4. https://doi.org/10.1109/oceanse.2007.4302310

Sarrazin, J., Rodier, P., Tivey, M. K., Singh, H., Schultz, A., & Sarradin, P. M. (2009). A dual sensor device to estimate fluid flow velocity at diffuse hydrothermal vents. *Deep Sea Research Part I: Oceanographic Research Papers*, *56*(11), 2065–2074. https://doi.org/10.1016/j.dsr.2009.06.008

Scheirer, D. S., Shank, T. M., & Fornari, D. J. (2006). Temperature variations at diffuse and focused flow hydrothermal vent sites along the northern East Pacific Rise. *Geochemistry, Geophysics, Geosystems*, *7*(3), Q03002. https://doi.org/10.1029/2005gc001094

Schultz, A., Delaney, J. R., & McDuff, R. E. (1992). On the partitioning of heat flux between diffuse and point source seafloor venting. *Journal of Geophysical Research*, *97*(B9), 12299–12314. https://doi.org/10.1029/92jb00889

Schultz, A., & Elderfield, H. (1994). Direct measurements of the physics and chemistry of diffuse flow and high-temperature effluent at TAG and Broken Spur vent fields.

Seyfried, W., & Bischoff, J. L. (1977). Hydrothermal transport of heavy metals by seawater: The role of seawater/basalt ratio. *Earth and Planetary Science Letters*, *34*(1), 71–77. https://doi.org/10.1016/0012-821x(77)90107-8

Simeoni, P., Sarrazin, J., Nouze, H., Sarradin, P.-M., ondreas, H., Scalabrin, C., & Sinquin, J.-M. (2007). Victor 6000: New high resolution tools for deep sea Research. Module de Mesures en Route; OCEANS 2007—Europe, 1–6. https://doi.org/10.1109/oceanse.2007.4302214

Singh, S. C., Crawford, W. C., Carton, H., Seher, T., Combier, V., Cannat, M., et al. (2006). Discovery of a magma chamber and faults beneath a Mid-Atlantic Ridge hydrothermal field. *Nature*, *442*(7106), 1029–1032. https://doi.org/10.1038/nature05105

Sohn, R. A. (2007). Stochastic analysis of exit fluid temperature records from the active TAG hydrothermal mound (Mid-Atlantic Ridge, 26°N): 1. Modes of variability and implications for subsurface flow. *Journal of Geophysical Research*, *112*(B7), B07101. https://doi.org/10.1029/2006jb004435

Sohn, R. A., & Harris, R. N. (2021). Spectral analysis of vertical temperature profile time-series data in Yellowstone Lake sediments. *Water Resources Research*, *57*(4), e2020WR028430. https://doi.org/10.1029/2020wr028430

Sturz, A., Itoh, M., & Smith, S. (1998). Proceedings of the ocean drilling program, 158 scientific results. *Proceedings of the Ocean Drilling Program*. https://doi.org/10.2973/odp.proc.sr.158.221.1998

Thomson, D. J. (1982). Spectrum estimation and harmonic analysis. *Proceedings of the IEEE*, *70*(9), 1055–1096. https://doi.org/10.1109/proc.1982.12433

Tivey, M. K. (1995). The influence of hydrothermal fluid composition and advection rates on black smoker chimney mineralogy: Insights from modeling transport and reaction. *Geochimica et Cosmochimica Acta*, *59*(10), 1933–1949. https://doi.org/10.1016/0016-7037(95)00118-2

Tivey, M. K. (2007). Generation of seafloor hydrothermal vent fluids and associated mineral deposits. *Oceanography*, *20*(1), 50–65. https://doi.org/10.5670/oceanog.2007.80

Tivey, M. K., Bradley, A. M., Joyce, T. M., & Kadko, D. (2002). Insights into tide-related variability at seafloor hydrothermal vents from time-series temperature measurements. *Earth and Planetary Science Letters*, *202*(3–4), 693–707. https://doi.org/10.1016/s0012-821x(02)00801-4

Tivey, M. K., & Delaney, J. R. (1986). Growth of large sulfide structures on the Endeavour segment of the Juan de Fuca ridge. *Earth and Planetary Science Letters*, *77*(3–4), 303–317. https://doi.org/10.1016/0012-821x(86)90142-1

von Damm, K. L. (1988). Systematics of and postulated controls on submarine hydrothermal solution chemistry. *Journal of Geophysical Research*, *93*(B5), 4551–4561. https://doi.org/10.1029/jb093ib05p04551

von Damm, K. L., Edmond, J. M., Grant, B., Measures, C. I., Walden, B., & Weiss, R. F. (1985). Chemistry of submarine hydrothermal solutions at 21°N, East Pacific Rise. *Geochimica et Cosmochimica Acta*, *49*(11), 2197–2220. https://doi.org/10.1016/0016-7037(85)90222-4

von Damm, K. L., & Lilley, M. D. (2004). In W. S. D. Wilcock (Ed.), *Diffuse flow fluids from 9° 50′N East Pacific Rise: Origin, evolution and biogeochemical controls*.

von Damm, K. V., Bray, A. M., Buttermore, L. G., & Oosting, S. E. (1998). The geochemical controls on vent fluids from the Lucky Strike vent field, Mid-Atlantic Ridge. *Earth and Planetary Science Letters*, *160*(3–4), 521–536. https://doi.org/10.1016/s0012-821x(98)00108-3

Waeles, M., Cotte, L., Pernet-Coudrier, B., Chavagnac, V., Cathalot, C., Leleu, T., et al. (2017). On the early fate of hydrothermal iron at deep-sea vents: A reassessment after in situ filtration. *Geophysical Research Letters*, *44*(9), 4233–4240. https://doi.org/10.1002/2017gl073315

Wilcock, W. S. D., & Delaney, J. R. (1996). Mid-ocean ridge sulfide deposits: Evidence for heat extraction from magma chambers or cracking fronts? *Earth and Planetary Science Letters*, *145*(1–4), 49–64. https://doi.org/10.1016/s0012-821x(96)00195-1

Xu, G., Larson, B. I., Bemis, K. G., & Lilley, M. D. (2017). A preliminary 1-D model investigation of tidal variations of temperature and chlorinity at the Grotto mound, Endeavour Segment, Juan de Fuca Ridge. *Geochemistry, Geophysics, Geosystems*, *18*(1), 75–92. https://doi.org/10.1002/2016gc006537